ELSEVIER

Journal of Fluids and Structures 25 (2009) 364–388

JOURNAL OF
FLUIDS AND
STRUCTURES

www.elsevier.com/locate/jfs

Generation of tones due to flow past a deep cavity: Effect of streamwise length

Y. Yang[a], D. Rockwell[a,*], K. Lai-Fook Cody[b], M. Pollack[b]

[a]*Department of Mechanical Engineering and Mechanics, 356 Packard Laboratory, Lehigh University,*
19 Memorial Drive West, Bethlehem, PA 18015-3095, USA
[b]*Lockheed-Martin, Schenectady, NY, USA*

Received 10 August 2006; accepted 20 May 2008
Available online 6 December 2008

Abstract

Shear flow past a deep cavity can generate self-sustained oscillations, including locked-on flow tones, due to coupling between the inherent instability of the separated shear layer and an acoustic mode of the cavity resonator. This investigation focuses on the dimensionless pressure amplitude response within a deep cavity, as a function of the streamwise length of the cavity opening; for each length, the pressure response is characterized over a wide range of dimensionless inflow velocity. Criteria for locked-on flow tones are assessed. They include a measure of the strength of lock-on, SoL and the quality factor Q. All self-excited oscillations are assessed using both of these criteria, in order to interpret dimensionless forms of the fluctuation pressure amplitude. The dimensionless pressure amplitude response of the cavity involves several successive regimes, due to variations of streamwise length L of the cavity opening. These regimes are defined in relation to L/θ, where θ is the momentum thickness of the inflow boundary layer. Below a minimum value of L/θ, flow tones cannot be generated. Furthermore, these regimes are defined in terms of the possible hydrodynamic modes (stages) of the unsteady shear layer and the acoustic modes of the deep cavity.

Keywords: Acoustics; Flow-acoustic coupling

---

1. Introduction

Flow-acoustic coupling, which involves coupling between a hydrodynamic mode (stage) of a separated shear layer and an acoustic mode of an adjacent resonator, occurs in a broad range of engineering applications. A brief overview of investigations, which are related to those of the present study, is given in the following.

1.1. Flow-acoustic coupling in engineering configurations

The instability of a separated shear layer serves as a hydrodynamic source, which can couple with one or more of the modes of an adjacent resonator. This concept, which is present in many different flow configurations, is reviewed by Rockwell and Naudascher (1978, 1979), Rockwell (1983, 1998), Blake (1986), Weaver et al. (2000), Rockwell et al.

---

[*] Corresponding author. Fax: +1 610 758 4041.
E-mail address: dor0@lehigh.edu (D. Rockwell).

0889-9746/$ - see front matter
doi:10.1016/j.jfluidstructs.2008.05.003

(2003), and Takeda and Shieh (2004). Previous investigations of flow past cavity configurations indicate that flow tones are attainable not only for rectangular cavities, but also for three-dimensional (nonrectangular) cavity geometries.

If one considers a broader range of flow configurations, in addition to a single cavity, it is evident that pronounced flow tones can occur. These configurations include jet excitation of a long (closed) organ pipe (Cremer and Ising, 1967; Fletcher, 1974, 1976, 1979), jet-sequential orifice plates (Howe, 1975, 1980; Flatau and Van Moorham, 1990; Hourigan et al., 1990), wake from a plate in a test section (Parker, 1966; Cumpsty and Whitehead, 1971; Stoneman et al., 1988), shear layer-cavity resonator (DeMetz and Farabee, 1977; Elder, 1978; Nelson et al., 1981, 1983), and cavity shear layer-long pipeline (Pfizenmaier, 1973; Schachenmann and Rockwell, 1980; Rockwell and Schachenmann, 1982a, b; Rockwell and Karadogan, 1982, 1983; Davies, 1981, 1996a b; Rockwell et al., 2003; Geveci et al., 2003; Oshkai et al., 2004). The configuration of a cavity shear layer-side branch (deep cavity) is not addressed in the foregoing. This configuration, which is of primary interest in the present study, is described in detail in the following sections.

1.2. Flow-acoustic coupling in single side branches

Of particular practical importance is the occurrence of flow-acoustic coupling that involves resonance of the side branch of the duct, which may, in some cases, couple with a resonant mode of the main duct. Ingard and Singhal (1976) characterize coupling phenomena involving modes of the side branch and the main duct. Bruggeman (1987) addressed several basic characteristics of a side-branch resonator in a main pipe (duct), and described the acoustic pressure in both the side branch and the main pipe, as well as the radiation condition at the exhaust of the pipe, which had an influence on the maximum attainable pressure amplitude at the dead end of the side-branch resonator. Many of these aspects are also described by Bruggeman et al. (1989, 1991). Ziada and Bühlmann (1992) address the case of a single side branch; in their experiments, the main duct extended to a long pipe with an absorption silencer, thereby limiting the pressure amplitude to very low values. Ziada and Bühlmann (1992) summarize the consequences of radiation, friction and heat losses on the amplitude of the pressure fluctuation at the dead end of the side branch, by in-depth consideration of the data of Jungowski et al. (1989), which indicate the importance of the ratio of the diameter of the side branch to the diameter of the main duct on the maximum attainable pressure amplitude at the end of the side branch. Hofmans (1998) provides quasi-steady and numerical models of a single side branch connected to a main duct, accounting for the direction of the mean flow and the acoustic flux of the side branch to the main duct. This numerical simulation provided insight into the amplitude of the pressure fluctuation at the dead end of the side branch, in relation to reflection conditions at the end of the main duct.

In contrast to the foregoing investigations involving a side-branch (deep cavity-main duct) configuration, Dequand et al. (2003a, b) considered the case of an isolated deep cavity exposed to the free atmosphere. Very strong flow tones were attainable for this configuration. Geometric changes of the cavity mouth (opening) were related to the amplitude of pulsation at the dead end of the deep cavity.

1.3. Flow-acoustic coupling in coaxial and tandem side branches

A coaxial side-branch system involves two side branches located in line with each other, on opposite sides of the main duct. Ziada and Bühlmann (1992) and Kriesels et al. (1995) demonstrate that large amplitudes of the fluctuating pressure at the dead ends of the side branches can be attained. It is generally accepted that radiation damping from each side branch is minimized for this coaxial configuration, which enhances the maximum attainable amplitude. Further aspects of oscillations in this configuration are addressed in the investigations of Radavich et al. (2001) and Dequand et al. (2003c).

A tandem side-branch configuration involves two successive side branches on the same side of the main duct. Bruggeman (1987), as well as Bruggeman et al. (1989, 1991), show that large pressure amplitudes can be attained at the dead end of the side branch, provided the spacing between the branches allows existence of a favorable phase relationship between them. This configuration was further investigated by Ziada and Bühlmann (1992).

1.4. Models and simulations

For the case of moderate to strong amplitudes of oscillation, the occurrence of flow tones has been modeled analytically by Bruggeman (1987), Kriesels et al. (1995), and Dequand et al. (2003a, b). For the limiting case of large amplitude oscillations, the central role of vortices, and the associated production of sound and nonlinear losses, has been addressed by Howe (1983). Related numerical simulations include those of Hofmans (1998), Radavich et al.

(2001), Ricot et al. (2002), Dequand et al. (2003b), and Mallick et al. (2003). (The authors are indebted to a referee for suggesting a number of the foregoing citations and their interpretation.)

1.5. *Unresolved issues*

On the basis of the state-of-the-art of oscillations due to side-branch resonators, which are described in the foregoing, it is possible to define a number of key issues that require clarification. They are briefly outlined in the following. In doing so, the terminology of an isolated deep cavity is intended to represent a deep cavity in absence of coupling effects with a main duct:

(a) The onset of a flow tone in an isolated deep cavity has not been addressed in terms of the streamwise length of the cavity opening in relation to the boundary layer thickness of the inflow. When all other parameters in the flow and acoustic system are held constant, it should be possible to find a critical value of dimensionless streamwise length at which the onset of the flow tone occurs.
(b) As the dimensionless length of the opening of the deep cavity is successively increased beyond the minimum value defined in (a), certain hydrodynamic modes (stages) of the shear layer along the cavity opening and detectable acoustic modes of the deep cavity will become distinctly defined. Furthermore, for certain of these combinations, the resonant coupling between them will be sufficient such that a coupled flow tone is generated. These phenomena have not been characterized. It should be possible to define regimes of response with increasing values of dimensionless streamwise cavity length, which incorporate detection of, and coupling between, definable hydrodynamic modes (stages) and acoustic modes.
(c) For a given value of dimensionless streamwise length of the cavity, a minimum critical velocity, for which the onset of a flow tone first occurs, should be defined. At values of velocity larger than this critical value, the manner in which resonant coupling occurs between the hydrodynamic modes (stages) and acoustic modes should be defined in detail.
(d) The criteria for defining the onset of a flow tone need to be assessed and compared with each other. Two possibilities include a strength of lock-on SoL criterion, which involves the amplitude of the pressure fluctuation at the dead end of the cavity, in excess of a reference (background) amplitude, and a quality Q factor of the spectral peak of the pressure fluctuation at the dead end of the cavity.

1.6. *Overview of investigation*

The rich variety of previous investigations described in the foregoing provides a basis for investigation of the resonant response characteristics of an isolated deep cavity, in absence of coupling effects with an adjacent (main) duct. Variations of streamwise length of the cavity, as well as depth of the cavity, will be considered, in relation to spectra of the pressure response as a function of flow velocity. These data will define the critical dimensionless velocity for onset of a flow tone (locked-on states) using different criteria. Moreover, the results of linear stability theory will be used to aid interpretation.

2. Experimental system and techniques

2.1. *Overview of experimental system*

All components of the experimental system, both upstream of, and including the main test section, were designed and fabricated in the Fluid Mechanics Laboratories at Lehigh University. Two principal subsystems comprise the overall experimental system. The first subsystem is the air conditioning and supply system, and the second is the actual inlet duct-deep cavity system. The first subsystem is located in a separate room, which is isolated from the room containing the inlet duct-deep cavity system. This approach allows isolation of undesirable mechanical vibrations and acoustic effects associated with the air compressor system.

A compressor maintains air at a pressure of 552–689 kPa (80–100 psig) in a plenum, which is stored in a compressed air plenum. At the outlet of the plenum, an air dryer arrangement allows separation of residual water from the air, and a filter system extracts foreign particles. The dried and filtered air is transmitted through the isolation wall into the room that houses the main experimental facility, i.e., the main duct—deep cavity arrangement with its associated plenum.

An overview of the main duct—deep cavity facility is provided in Fig. 1. It consists of an arrangement of valves, an inlet plenum, three-dimensional nozzle, which precedes a rectangular cross-section main duct that is terminated by the deep cavity.

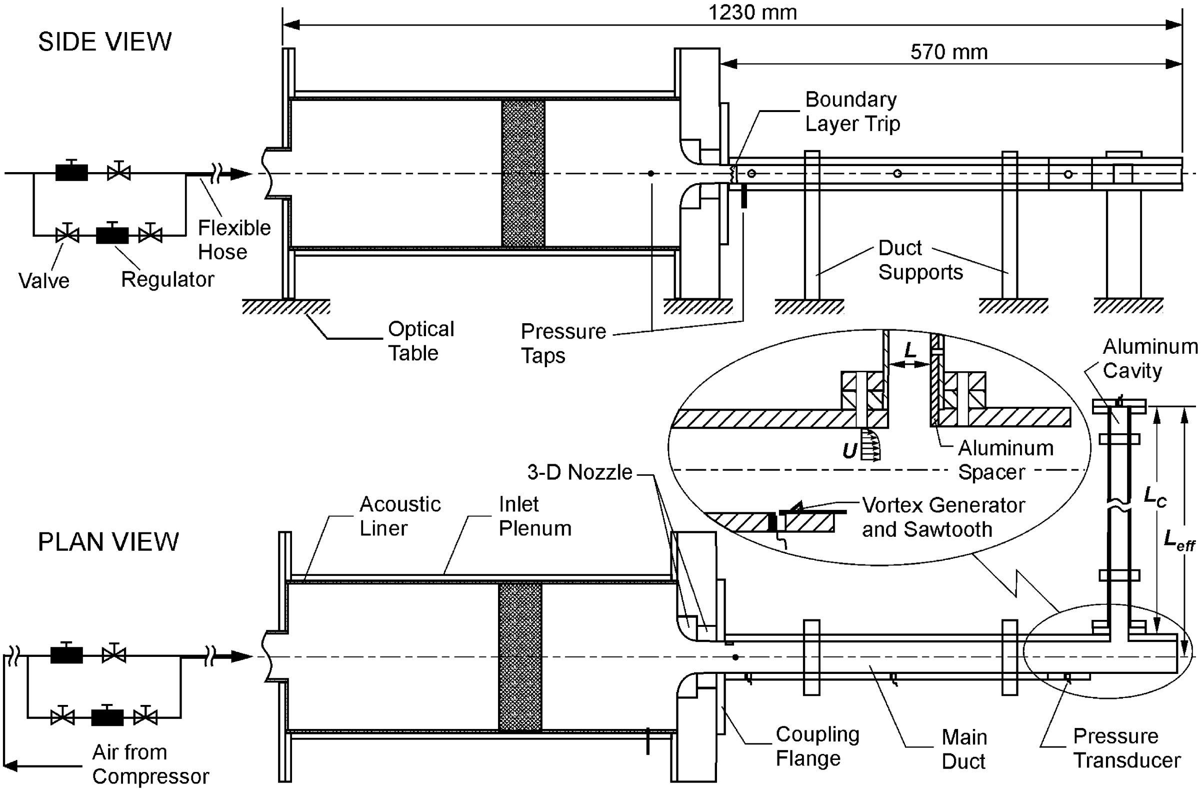

Fig. 1. Overview of deep cavity facility.

The system of valves and regulators shown at the left of Fig. 1 is made up of a throughflow and a bypass arrangement. This dual path for the incoming air allows a wide range of mass flow rates. The flow from the valve-regulator systems passes through a long flexible hose, which has an inside diameter of 25.4 mm and a total length of 5 m. It was found that this longer hose very effectively attenuated high-frequency disturbances generated by the valve-regulator system. The downstream end of this flexible hose was connected to the inflow port of the inlet plenum. Within the plenum, the airflow expanded, passed through a flow conditioner (honeycomb), then was accelerated in a three-dimensional nozzle, which, in turn, fed into the main duct.

The entire inlet plenum–nozzle–main duct-deep cavity system was located in a room having dimensions 6 m wide × 9 m long and a height of 4.5 m. The test facility was located approximately in the middle of the room, on a rigid table, at an elevation of 0.5 m above the floor of the room. Extensive preliminary experiments employing an absorptive chamber around the test section showed that peaks in representative spectra due to flow-acoustic coupling were associated only with the modes of the deep cavity resonator. No spurious peaks due to possible room acoustics were detected. This chamber had various shapes and dimensions, including a rectangular chamber having a width of 241 mm, a length of 413 mm, and a height of 178 mm.

In the following, the components of the main duct-deep cavity system are described in detail.

2.2. Main test section

2.2.1. Inlet plenum

The inlet plenum of the main duct-deep cavity system, as shown in Fig. 1, was constructed entirely of plexiglas. A honeycomb system located within the plenum attenuates flow disturbances. The interior surface of the plenum is lined with acoustic damping foam, in order to attenuate the local acoustic resonances.

2.2.2. Three-dimensional nozzle

A three-dimensional nozzle was connected to the exit of the plenum. It was manufactured using a rapid prototyping technique, and designed to optimize the acceleration of flow from a relatively low velocity in the plenum to a high velocity at the inlet of the main duct. The velocity U was calculated using the standard relationship that relates total pressure to the sum of static and dynamic pressure. Correction for compressibility at higher velocities was not applied. The upper limit of uncertainty of the velocity of the measurement of U is 3%. The internal dimensions of the exit of the three-dimensional nozzle matched the dimensions of the inlet of the main duct. These dimensions are given in the next section.

2.2.3. *Main duct subsystem*

The main duct, which was attached to the exit of the three-dimensional nozzle described in the preceding subsection, is shown in Fig. 1. The internal dimensions of this duct were 38.1 mm × 25.4 mm. The downstream end of the duct exhausted into the open atmosphere. Moreover, the duct was bounded on three sides over its entire length of 570 mm, except for one side on the open end, which is evident in the close-up of Fig. 1. This open side allowed decoupling of the flow through the main duct and the resonance of the deep cavity. Other features of the main duct arrangement include a boundary layer trip, which involved a rectangular bar of streamwise length 5 mm and height 1.5 mm, in order to promote transition of the boundary layer emanating from the three-dimensional nozzle. A static pressure tap was located immediately downstream of the boundary layer trip, in order to provide a reference steady pressure for measurement of flow rate through the main duct.

Near the downstream end of the duct, a vortex generator and sawtooth plate were located at the separation lip shown in the close-up of Fig. 1. The purpose of this arrangement was to attenuate the process of vortex formation from the lip of the duct end. The effectiveness of this arrangement was verified by spectra of hot wire measurements, as well as detailed quantitative images of the flow structure. These approaches show that no coherent vortex formation occurred downstream of this edge of the duct. In essence, this arrangement was effective for two primary reasons: the vortex generator yielded patterns of streamwise vorticity; and, furthermore, the sawtooth arrangement prevented the effective conversion of the disturbances from the radiated acoustic wave front to spanwise coherent vorticity concentrations at the lip. The vortex generator had protrusions of height 5 mm; these triangular protrusions were at an angle of 45° with respect to the incident free stream. Moreover, they had a wavelength of 8 mm along the span of the duct. The saw tooth extension had a peak to trough distance of 5 mm and a spanwise wavelength of 8 mm. The crests of the sawtooth arrangement protruded a distance of 7 mm from the lip of the main duct.

The locations for three flush-mounted pressure transducers are indicated in the plan view of Fig. 1. These pressure transducers were employed to monitor the amplitude and frequency of organized spectral components within the main duct, in order to ensure that negligible coupling occurred between the main duct and the deep cavity.

2.2.4. *Deep cavity arrangement*

Details of the deep cavity are shown in the plan view and the close-up of Fig. 1. The cavity duct, oriented horizontally, is made of an aluminum tube, which is of a rectangular cross-section, with wall thickness of 3.2 mm. The total depth of the cavity is designated as L_C. This total depth involves the sum of the actual cavity duct and a plexiglas spacer, along with the thickness of the main duct. The plexiglas spacer is located between the flange of the cavity duct and the wall of the main duct. For the present investigation, the total depth is fixed at $L_C = 482.6$ mm. The cavity also has a fixed width of 25.4 m. The length L of the cavity opening had values of 25.4, 50.8, and 76.2 mm. Smaller values of L were attained by fixing aluminum plate spacers within the deep cavity rigidly. These spacers extended over the entire depth of the main cavity and were screwed to the wall of the cavity.

The end of the deep cavity was terminated by an aluminum endplate having a thickness of 12.7 mm. It housed a PCB pressure transducer, which will be described in the following subsection.

Dequand et al. (2003a, b) and Hofmans (1998) bring forth the possible effect of wall vibrations on the amplitude response characteristics of a resonator, among other possible sources of discrepancy between their measurements and simulations. Their pressure amplitudes are, however, very large. In the investigation of Dequand et al. (2003c), the representative amplitude ranges from 1 to 2 orders of magnitude larger than in the present investigation. Lambert (1953) has determined the effect of wall thickness on the damping of a closed, tube. The range of wall thickness considered therein includes the thickness of the present wall of the duct of rectangular cross-section. In his investigation, wall vibration contributed only about 4% to the total absorption loss. Finally, in the present investigation, additional experiments were conducted by clamping 9 mm thick aluminum slabs against the exterior wall of a representative ($L_C = 482.6$ mm) cavity. No detectable difference in the three-dimensional (p–f–U) response plot was discernible over the entire range of U.

The naturally generated boundary layer was characterized at a location immediately upstream of the leading edge of the cavity opening, i.e., at a distance of 8 mm upstream of the leading edge of the cavity. This location corresponds to the profile of time-averaged streamwise velocity in the close-up of Fig. 1. The acquisition of such velocity profiles at different values of mean inflow velocity U is accomplished using a total pressure probe and a static wall tap (not shown). Then the values of momentum thickness θ are determined from these profiles in relation to U. Experimental results show that variation of momentum thickness θ closely follows the one-fifth law of a turbulent boundary layer. Specifically, $\theta = C/U^{1/5}$, where θ is in m and inflow velocity U is in m/s, and $C = 1.154 \times 10^{-3}\,\mathrm{m}^{6/4}/\mathrm{s}^{1/5}$. Therefore, this analytical expression is employed throughout the present investigation to evaluate the inflow boundary layer momentum thickness θ.

2.2.5. Main duct—deep cavity system: decoupling of acoustic characteristics

An essential aspect of the design of the main duct and the deep cavity described in the preceding subsection is that they have different resonant frequencies, in order to minimize possible coupling between these two major components. A central consideration is that the resonance of the main duct does not influence the resonance of the deep cavity. All self-excited components determined during experiments are directly traceable to excitation of the deep cavity. It is worth noting that theoretically determined resonant frequencies based on the cavity depth L_C do not match experimental values, due to the complexity of the acoustic field in the proximity of the cavity mouth. By adding an end correction of 19.1 mm to each value of L_C, however, such discrepancies disappear. The corrected cavity depth is designated as L_{eff}, which is shown in the plan view of Fig. 1.

2.3. Acquisition and processing of pressure data

2.3.1. Pressure transducers

High-sensitivity, flush-mounted PCB pressure transducers (Model no. U103A02) were employed; they had a nominal sensitivity of 1727 mV/psi. The outputs from the transducers were connected to a multi-channel signal conditioner. This multi-channel conditioner allowed independent adjustment of the gains of the pressure transducer signals. Generally speaking, however, it was possible to employ the same value of gain for all pressure measurements. This gain adjustment is important in order to meet the required voltage input levels of the analog/digital (A/D) board.

2.3.2. Acquisition of pressure signals

The conditioned pressure signals were transmitted to ports on a data acquisition board with 12-bit resolution. This board, when operating in the single channel acquisition mode, can sample at the rate of $250KS/\mathrm{s}$, in which $K = 10^3$ and S is the number of samples. In the present scenario, a total of eight channels (four connected to pressure transducers and four empty) were employed, so the effective sampling rate is reduced by a factor of eight, i.e., it takes on a value of $31KS/\mathrm{s}$ per channel. In essence, there are two considerations to determine whether this sampling rate is adequate. First of all, for characterization of pressure in the frequency domain, the sampling rate should be at least twice the maximum frequency of interest. For representations in the time domain, a minimum of five samples per cycle is required, but a minimum of ten samples per cycle is desirable. Considering these requirements together, the acquisition system should have a sampling rate at least ten times as high as the maximum typical frequency of interest in the present investigation, which corresponds to a sampling rate of approximately 1.7×10^4 Hz. This requirement is approximately a factor of two lower than the acquisition rate of $31KS/\mathrm{s}$ per channel. It is also important to realize that this type of board basically consists of one A/D converter, and the acquisition of eight pressure signals is accomplished using a multiplexing technique. The scan interval is defined as the time required going from a recorded point corresponding to pressure transducer no. 1, through the sequence of the other transducers, and return to the channel of transducer no. 1. This scan interval is basically the inverse of the maximum data acquisition rate per channel is $1/(31.25 \times 10^3)$, which corresponds approximately to 32 ms.

2.3.3. Processing of pressure signals

LabView software was used to process the pressure transducer signals. The major parameters for spectral analysis using the fast Fourier transform (FFT) must be properly defined so that adequate resolution in the frequency domain is accomplished, while at the same time minimizing the amount of collected data. In order to determine which values of each parameter were adequate, a series of averaging tests were performed using broadband noise input. For a given set of parameters, the number of averaged files was varied to determine the minimum number of files and, hence, the minimum number of data samples needed to properly represent the system response.

The parameters were as follows: (i) the number of samples acquired per data set; (ii) the sampling rate; and (iii) the number of data sets employed to obtain an average. The sampling rate must be twice as high as the maximum frequency of interest. Therefore, the necessary sampling rate varied directly with the maximum frequency of interest for each experiment. The value of the frequency resolution (Δf) is equal to the sampling rate (f_s) divided by the number of samples per data set (n_s). Once the sampling rate was determined for each experiment, the number of samples was calculated according to $n_s = f_s/\Delta f$.

In order to determine the value for Δf, another set of averaging experiments was performed. Values of Δf were varied. These tests showed that $\Delta f = 0.5$ Hz adequately characterized the system response, while providing acceptable frequency resolution at both the low and high ends of the frequency range of interest to these experiments. At the lowest and highest frequencies of interest, approximately 42 and 1665 Hz, $\Delta f/f$ has its maximum and minimum values of 0.012 and 0.0003, respectively.

During acquisition of final experimental data, the sampling rate was set to 4096 samples per second, which resulted in a Nyquist frequency of 2048 Hz, well above the maximum frequency component of interest for this research, which was approximately 1700 Hz. The number of samples per data set (n_s) was then specified, while maintaining $\Delta f = 0.5$ Hz, resulting in $2^{13} = 8192$ samples per data set. Each of the spectra represented herein was obtained by averaging a total of 40 data sets. Furthermore, the convergence of the calculated spectra as a function of the number of averaged spectra was undertaken using the band-limited white noise technique of loudspeaker excitation. This process was employed for a number of selected resonant modes of a deep cavity. Generally speaking, as few as ten averages yielded a peak spectral amplitude that was indistinguishable from the value determined from a larger number of averages, up to a total of one hundred averages, within an uncertainty of 5%. The pressure amplitude is expressed in terms of actual amplitude, as opposed to root-mean-square amplitude.

3. Onset and development of flow tones: pressure response characteristics

To determine the effect of streamwise length of the cavity opening on the generation of flow tones, a series of cavities having the same depth but various streamwise lengths were employed during experiments. The cavity depths are fixed at a moderate value of $L_C = 482.6$ mm, which, with the end correction, corresponds to an effective cavity depth of $L_{\text{eff}} = 501.7$ mm. The cavity lengths vary over the range from $L = 12.7$ to 76.2 mm.

3.1. Methods of presentation of data

In general, the occurrence of flow tones is directly related to the effectiveness of flow-acoustic coupling. Fig. 2 illustrates basic concepts as a basis for defining the terminology employed herein. From an acoustic perspective, to excite an acoustic resonance in a deep cavity, the incident and reflected waves must form a standing wave along the cavity, and this standing wave must have a pressure node at the open end and a pressure antinode at the dead end. As shown in Fig. 2(a), a quarter wave satisfies these conditions, and thus represents an acoustic resonant mode, namely the $a1$ mode. Similarly, a three-quarter wave ($a2$), a five-quarter wave ($a3$), and so on are also admissible.

The separated shear layer along the mouth of the cavity is susceptible to excitation over a broad range of frequencies, in accord with the linear stability theory of Michalke (1965) and the extensive experimental studies of convectively unstable free shear layers summarized by Ho and Huerre (1984). The frequency of the resonant mode of the cavity corresponds to the frequency of excitation of the separated shear layer, and the coherence of the instability is enhanced by the feedback loop, i.e., the upstream influence from the impingement corner of the cavity. This process therefore represents the origin of the acoustic resonance. The amplified instability, which may take the form of a vortical structure(s), feeds energy into the acoustic field, which then perturbs the separated shear layer, and so on. When the resonant-coupled oscillation has evolved to its steady state limit cycle, it is sustained according to the concept of Howe's (1975, 1980) acoustic power integral. This integral involves the instantaneous vorticity, which principally resides in the vortical structures, velocity fluctuations associated with the hydrodynamic field, and velocity fluctuations associated with the acoustic field. In essence, acoustic power is effectively generated when there exists a proper phase relationship between the vortical structure at the trailing edge of the cavity, and the phase and direction of the acoustic particle velocity in that region. This concept is physically interpreted by Hourigan et al. (1990).

Quantitative imaging of the shear layer along the mouth of the cavity, using high-image-density particle image velocimetry, showed the existence of either one, two, or three distinct vortical structures, designated as hydrodynamic modes $h1$, $h2$, and $h3$, respectively. Modes $h1$ and $h2$ are indicated in the schematics of Figs. 2(b) and (c), respectively, whereas Figs. 2(d)–(f) show patterns of instantaneous velocity V and vorticity ω corresponding to modes $h1$, $h2$, and $h3$.

To characterize the flow tone behavior, for a given cavity, and at a given inflow velocity, a time trace of pressure response at the dead end of the cavity was recorded. Then this measurement is presented in the frequency domain as an amplitude spectrum. A total of approximately 69 spectra were acquired, with each spectrum corresponding to a specified inflow velocity.

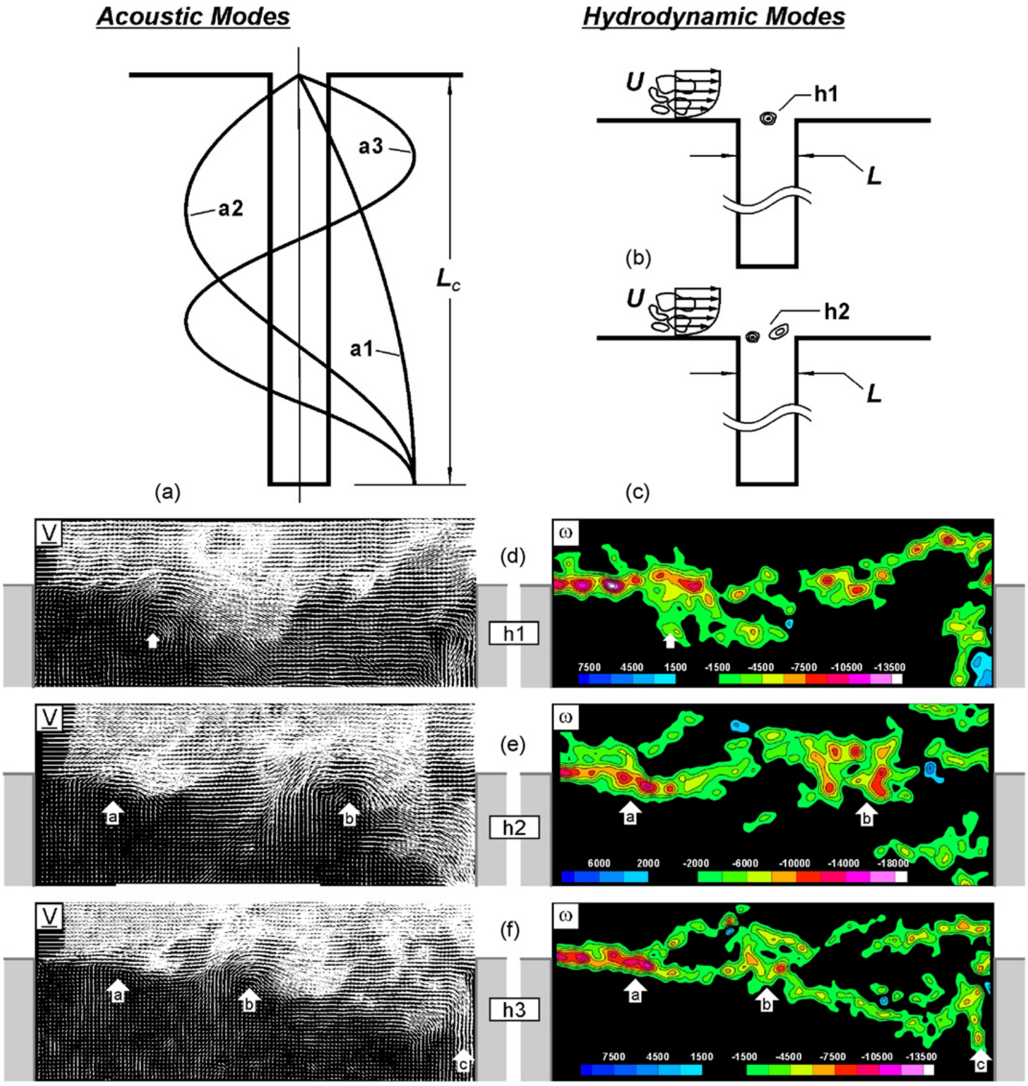

Fig. 2. Schematics demonstrating acoustic modes (a) and hydrodynamic modes (b, c), and patterns of instantaneous velocity V and vorticity ω corresponding to hydrodynamic modes $h1$, $h2$ and $h3$ (d–f).

It is insightful to employ a unified and comprehensive means of presentation and interpretation of families of these spectra. Use of a color-coded, isometric view, as given in the top plot of Fig. 3(c) (to be discussed in Section 3.2), was constructed for this purpose. In this type of plot, the magnitudes of the pressure are color-coded. This allows inspection of variations of color in two-dimensional space, in turn yielding an overview of the conditions corresponding to generation of relatively high-pressure amplitudes. The emphasis of the present investigation is on characterization for the onset of flow tones; therefore, the largest variations of color level occur at lower values of pressure amplitude. It is important to recognize that, when a threshold value of amplitude is exceeded, the same color (white) magnitude is maintained for all higher values of amplitude. It is therefore not possible to determine, in certain cases, the maximum amplitude of the pressure spectra based on three-dimensional color plots.

The aforementioned isometric color plots, such as the one shown in the top plot of Fig. 3(c), show crests along approximately constant values of dimensionless frequency, i.e., the Helmholtz number. These crests are related to acoustic resonance along the deep cavity, with each of them representing an acoustic *a* mode. Along each crest, there are also well-defined amplitude peaks. These peaks are caused by the interaction, or coupling, between an acoustic resonance and an instability mode of the shear layer; each peak corresponds to a flow tone.

In addition to the three-dimensional color plot, a corresponding plan view is also provided. This view allows straightforward designation of the hydrodynamic h and acoustic a mode of each of the peaks, as well as linear fits through these peaks in order to determine dimensionless values of frequency, e.g., Strouhal number. These types of designations are, for example, evident in the bottom plot of Fig. 3(c).

3.2. Effect of length of cavity opening at moderate cavity depth

The effect of variations of the length L of the cavity opening, at a constant value of cavity depth, $L_C = 482.6\,\text{mm}$, is given in Figs. 3(a)–(e). This series of experiments allows identification of the minimum value of L at which flow tones can be generated and, furthermore, provides characterization of the flow tones at relatively large values of length L of the cavity opening. In the descriptions that follow, the Q factor is employed as an index of the degree of lock-on. The Q

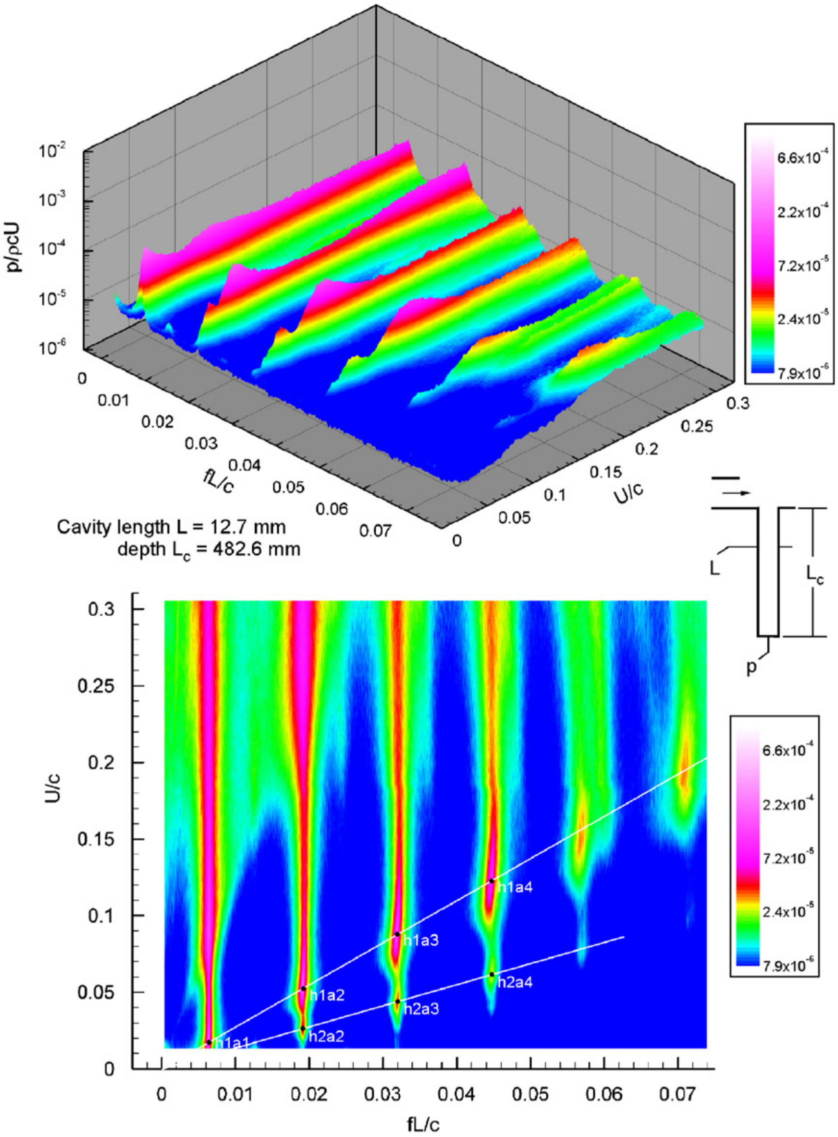

Fig. 3a. Three-dimensional (top) and plan (bottom) views of dimensionless pressure amplitude ($p/\rho cU$) on a logarithmic scale as a function of dimensionless frequency (fL/c) and dimensionless velocity (U/c). Dimensionless velocity is varied while cavity geometry remains fixed. The plots were constructed from individual spectra of the dimensionless pressure fluctuation at discrete values of dimensionless velocity. Cavity length L and depth L_C are $L = 12.7\,\text{mm}$ and $L_C = 482.6\,\text{mm}$.

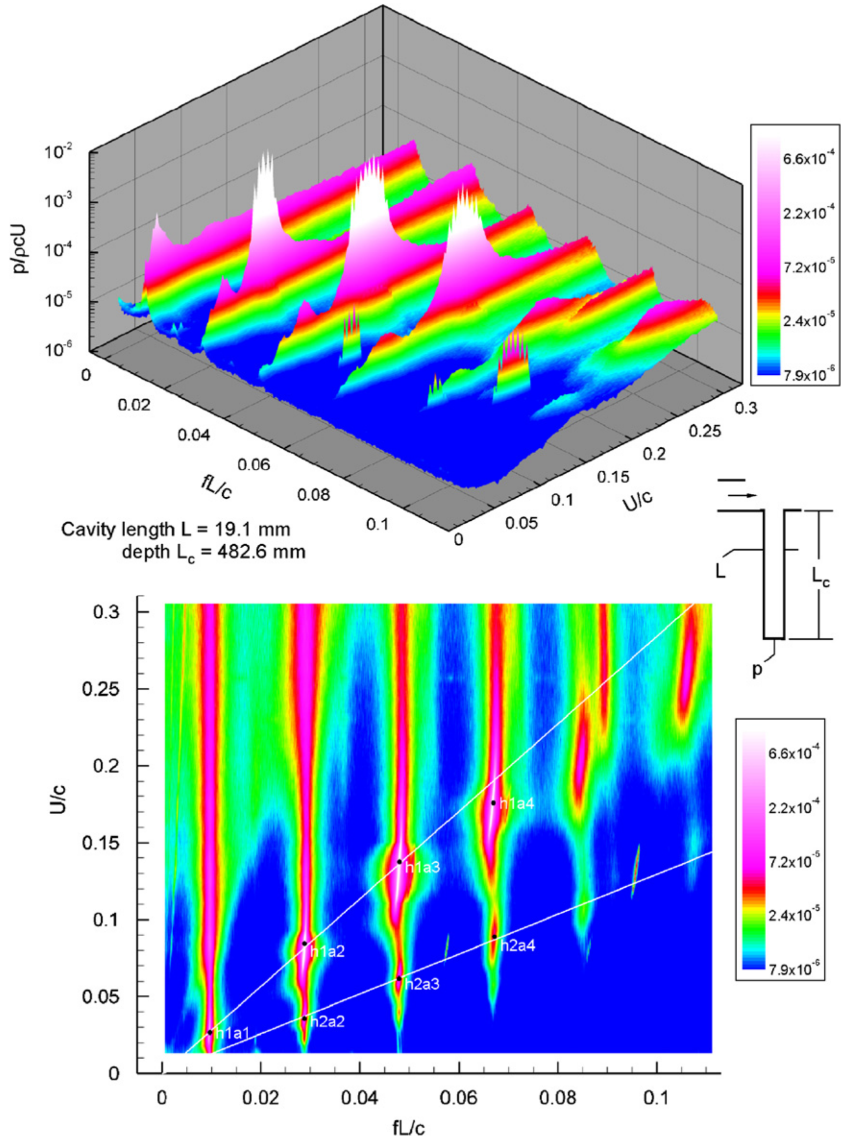

Fig. 3b. Three-dimensional (top) and plan (bottom) views of dimensionless pressure amplitude ($p/\rho cU$) on a logarithmic scale as a function of dimensionless frequency (fL/c) and dimensionless velocity (U/c). Dimensionless velocity is varied while cavity geometry remains fixed. Cavity length L and depth L_C are $L = 19.1$ mm and $L_C = 482.6$ mm.

factor is defined as $Q = f_0/(f_2 - f_1)$, in which f_0 is the frequency of the tone, and f_1 and f_2 are the frequencies at the half-power points of the spectral peak. It should be noted that the Q factor has significant uncertainty due to the finite frequency resolution Δf. A curve fitting procedure was employed during the evaluation of the Q factor to mitigate this uncertainty, so that it remained within 20%.

For the smallest value of length L of the cavity opening of $L = 12.7$ mm, Fig. 3(a) shows isometric and plan views of dimensionless pressure amplitude $p/\rho cU$ in logarithmic scale on a plane of dimensionless frequency fL/c versus dimensionless inflow velocity U/c. In these dimensionless forms, which are employed throughout the paper, ρ is density, and c is the speed of sound. It is evident that sharply defined peaks do not occur in Fig. 3(a), which suggests the lack of generation of a flow tone. In both the isometric and plan views, however, the excitation of the acoustic modes is indeed evident. These modes are represented by crests on the isometric view and strips on the plan view, respectively.

Although sharply defined peaks are not evident at this small value of L, relatively broad, low-amplitude peaks are evident, and a linear fit through them is given by the thin white line as shown on the plan view of Fig. 3(a). At the

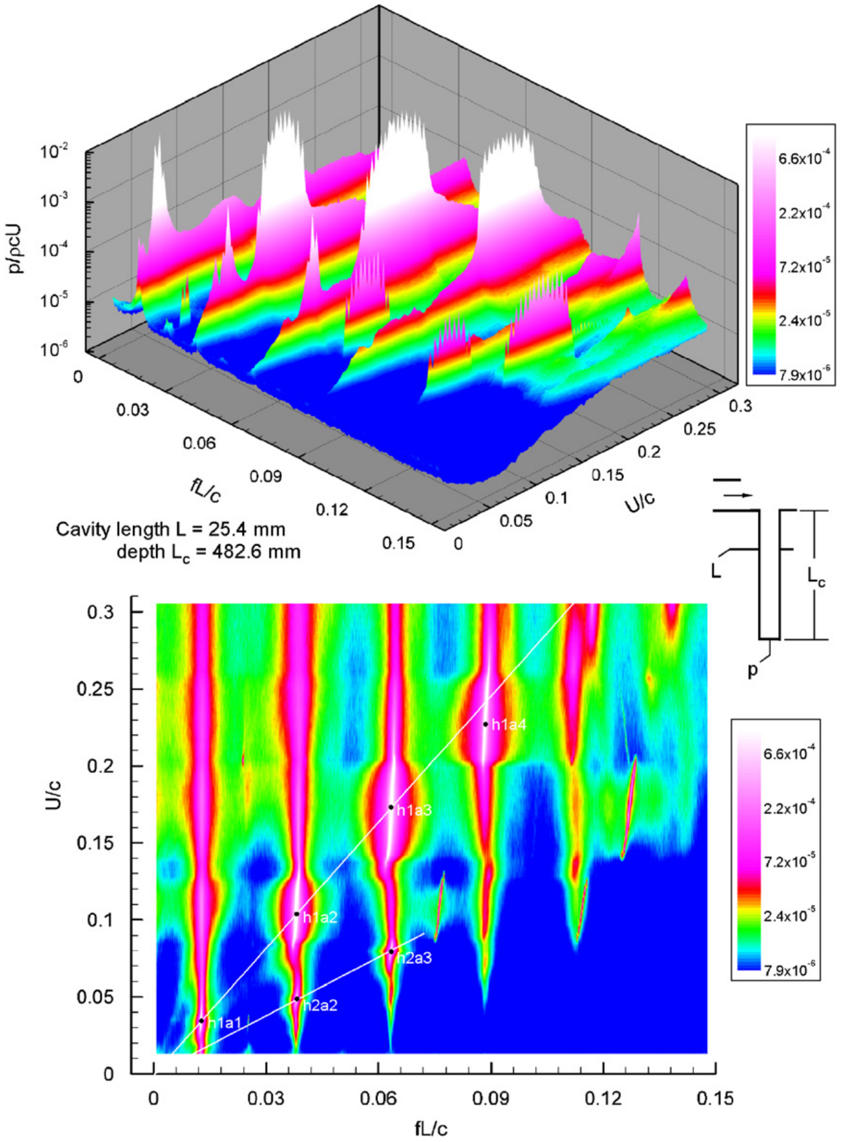

Fig. 3c. Three-dimensional (top) and plan (bottom) views of dimensionless pressure amplitude ($p/\rho cU$) on a logarithmic scale as a function of dimensionless frequency (fL/c) and dimensionless velocity (U/c). Dimensionless velocity is varied while cavity geometry remains fixed. Cavity length L and depth L_C are $L = 25.4$ mm and $L_C = 482.6$ mm.

location of each of these peaks, the corresponding hydrodynamic and acoustic modes are indicated. For example, $h1$ represents the first hydrodynamic mode and $a1$ represents the first acoustic mode. Evaluation indicates that the values of Q factor of these peaks are very low, ranging from 40 to 130.

A further increase of length L of the cavity opening to $L = 19.1$ mm is represented by the plots of Fig. 3(b). In this figure, it is evident that sharply defined peaks now occur, in contrast to the relatively broad peaks of the isometric views of Fig. 3(a). The plan view of Fig. 3(b) shows the clearly defined intersection of the hydrodynamic h and acoustic a modes, it is clear that the first two hydrodynamic modes (stages), i.e., $h1$ and $h2$ are clearly identifiable.

Correspondingly, very large values of Q are attained. They occur for the first hydrodynamic mode $h1$, especially when it occurs in conjunction with the second, third and fourth acoustic modes, i.e., $h1a2$, $h1a3$, and $h1a4$. On the other hand, although the second hydrodynamic mode $h2$ is detectable, its occurrence with the second, third, and fourth acoustic modes yields only relatively low values of Q factor, the largest being $Q = 140$ at $h2a3$.

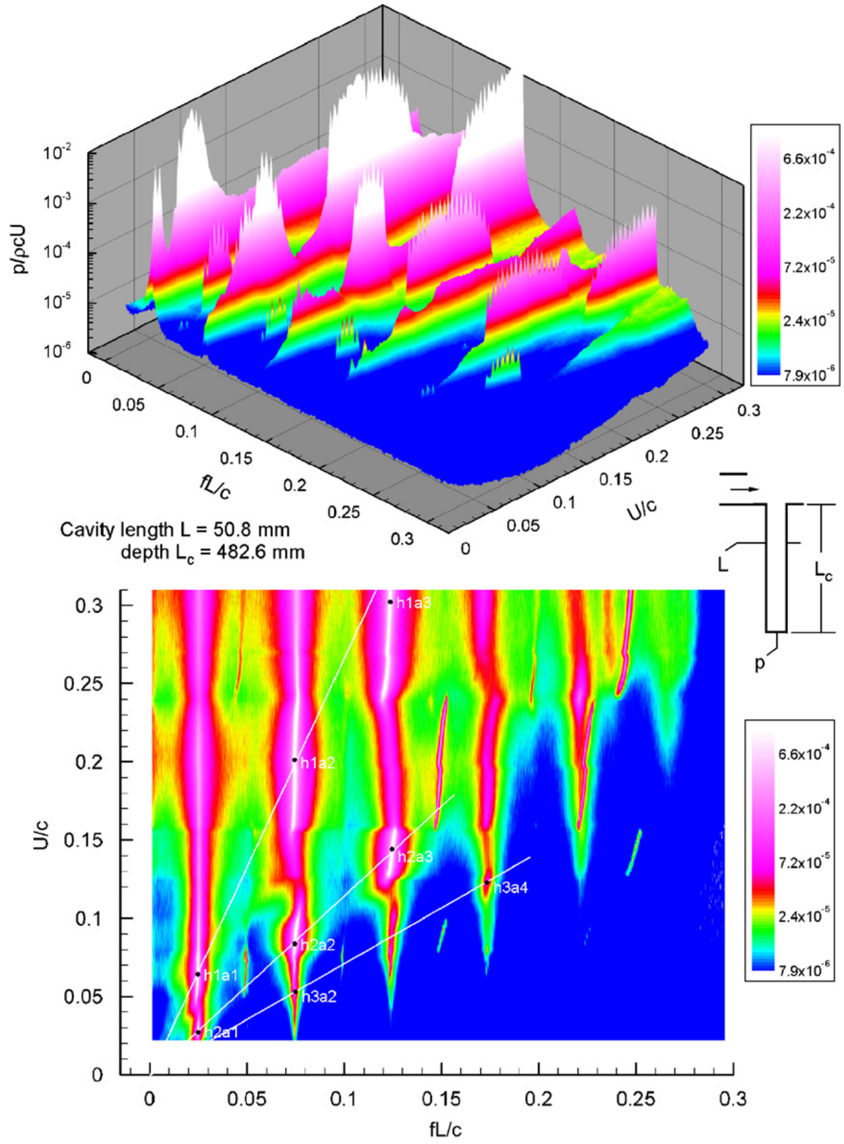

Fig. 3d. Three-dimensional (top) and plan (bottom) views of dimensionless pressure amplitude ($p/\rho cU$) on a logarithmic scale as a function of dimensionless frequency (fL/c) and dimensionless velocity (U/c). Dimensionless velocity is varied while cavity geometry remains fixed. Cavity length L and depth L_C are $L = 50.8$ mm and $L_C = 482.6$ mm.

The maximum values of Q of the order of $Q = 2000$–2600 are, in fact, the largest values attainable, even for further increases in length L of the cavity opening. It therefore appears that this value of $L = 19.1$ mm represents the case of the strongest coupling between the hydrodynamic instability of the shear layer associated with the acoustic a mode of the cavity resonator. A minimum value of L is required in order to allow the instability to adequately develop in the streamwise direction, and when this value of L is achieved, it is expected that optimal coupling will occur.

The next higher value of L of the cavity opening, $L = 25.4$ mm, is represented in Fig. 3(c). On the isometric view of Fig. 3(c), the peaks are sharply defined. On the plan view, the first and second hydrodynamic modes $h1$ and $h2$ are as indicated. It is evident that values of very high Q, which were evident for the previous case, $L = 19.1$ mm, persist. Again, values of Q of the order of 2000 are attainable for the first hydrodynamic mode $h1$. Furthermore, the values of Q for the second hydrodynamic mode have become substantial. For example, for the intersection of the second hydrodynamic mode and the second acoustic mode $h2a3$, as well as with the third mode $h2a3$, values of $Q = 620$ and 980 are attained.

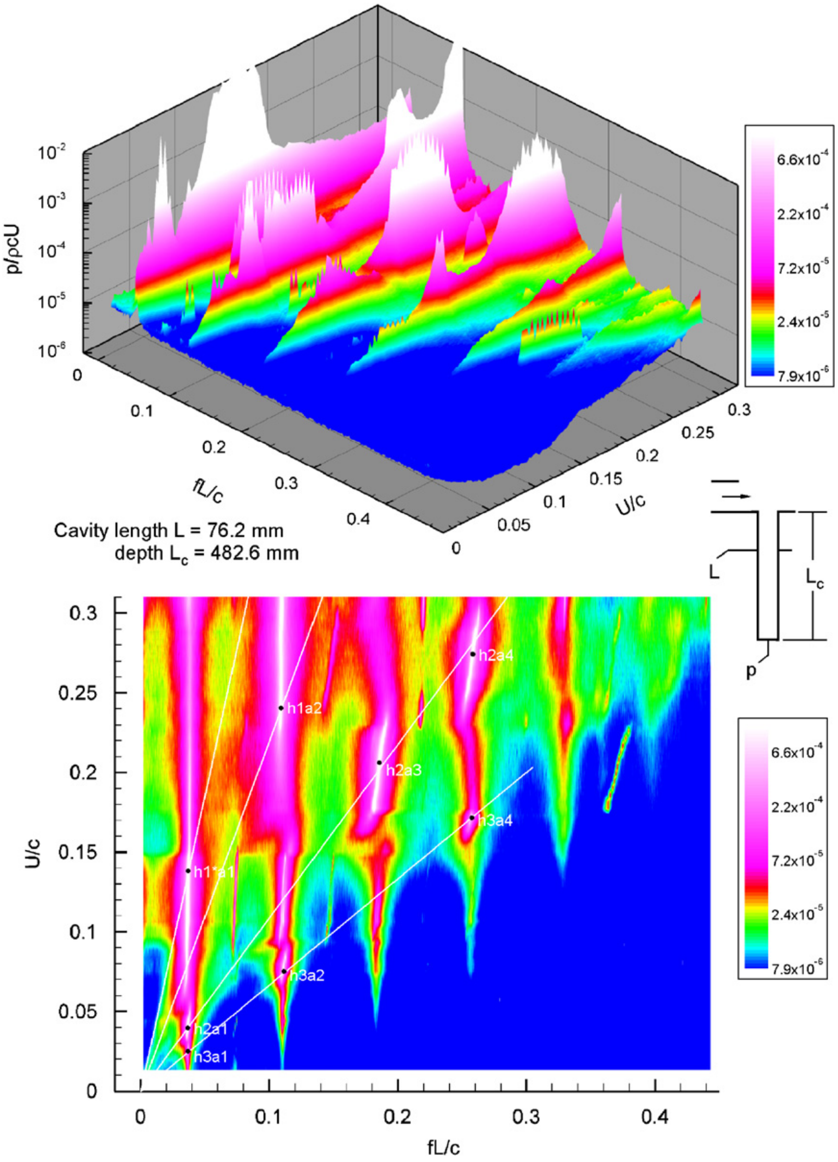

Fig. 3e. Three-dimensional (top) and plan (bottom) views of dimensionless pressure amplitude ($p/\rho cU$) on a logarithmic scale as a function of dimensionless frequency (fL/c) and dimensionless velocity (U/c). Dimensionless velocity is varied while cavity geometry remains fixed. Cavity length L and depth L_C are $L = 76.2$ mm and $L_C = 482.6$ mm.

Therefore, this longer value of cavity length has promoted much more sharply defined peaks of the second hydrodynamic mode.

A still larger value of length L of the cavity opening, $L = 50.8$ mm, is represented in the plots of Fig. 3(d). As indicated in the plan view, it is now possible to define three hydrodynamic modes $h1$–$h3$. For the first hydrodynamic mode $h1$, regions of relatively high $p/\rho cU$ extend over the entire range of U/c. In contrast, the second mode $h2$ is excited over successively smaller ranges of U/c, with lower values of peak amplitude. Close inspection of the plan view of Figs. 3(d) indicates that the third hydrodynamic mode $h3$ is indeed detectable, and is therefore included in the present assessment.

Evaluation of the Q factor indicates that for the first hydrodynamic mode $h1$, the values of Q generally remain large, with the maximum value of Q of the order of $Q = 1800$. But, on the average, these values are somewhat lower than for the previous (smaller) two values of L. On the other hand, for the second hydrodynamic mode $h2$, the values of Q have increased substantially to values of Q of the order of 1000–1300, which are significantly larger than the values of Q at the previous two smaller values of length L. Regarding the third hydrodynamic mode $h3$, values of Q generally remain small. We therefore witness the increasing predominance of the second hydrodynamic mode as it couples with respective values of acoustic modes a, in particular, $h2a2$ and $h2a3$.

The largest value of length $L = 76.2\,\text{mm}$ is indicated in Fig. 3(e). The basic form of the isometric plot of Fig. 3(e) shows a fundamental change, relative to the form for smaller values of length L. A strong excitation occurs at a relatively low dimensionless frequency of $fL/c = 0.0372$. Not only are the peak amplitudes large, but they extend over a substantial range of U/c and, in fact, are triggered at a relatively low value of $U/c = 0.087$.

The plan view of Fig. 3(e) shows a series of four hydrodynamic modes. The classical three modes $h1$, $h2$, and $h3$ are designated. In addition, a low-frequency mode $h1^*$ occurs at a low frequency relative to the mode $h1$. This mode $h1^*$ may be viewed as an extension of the mode $h1$. Its substantially lower frequency is due to the large amplitude excursions of the developing vortex deep into the cavity, as revealed by flow visualization, not addressed herein.

The values of Q for the first hydrodynamic mode $h1$ have degenerated to substantially lower values relative to those at smaller values of length L of the cavity opening. In the second hydrodynamic mode, $h2$, relatively high values of Q persist; that is, Q of the order of 1000 is attainable. Important, however, is the fact that in the third hydrodynamic mode, $h3$, a relatively high value of $Q = 760$ is now attainable. This longer cavity length has apparently allowed nearly full evolution of the third hydrodynamic stage $h3$, and thereby a strongly coupled oscillation leading to a high value of Q.

Regarding the special low-frequency mode, which is designated herein as $h1^*$, though it has a relatively large value of pressure amplitude p, its Q factor is not large, i.e., $Q = 330$.

The teeth-like structure of the large amplitudes in Figs. 3(b)–(e) is due to the incremental dimensionless velocity $\Delta(U/c)$ at which individual spectra were acquired, in conjunction with the frequency shift of loci of peak amplitudes. The software employed for construction of these three-dimensional plots does not smooth out this discretization effect, and no artificial means of smoothing were employed. Moreover, a similar teeth-like structure is observed in the published experiments of Rockwell et al. (2003), which involved a completely different configuration of a small cavity in a very long pipe system, connected at one end to a plenum and free at the other end. Complementary experiments involving various absorptive chamber arrangements at the termination of the pipe produced no detectable change in the spectra and the associated three-dimensional plots shown in the investigation.

An overview of the major pressure response peaks for the aforementioned values of length L of the cavity opening, as well as two additional values of L covered in the present investigation but not presented in the foregoing, is given in Fig. 4. For a given value of streamwise length L, all pressure response peaks are superposed on the same coordinates $p/\rho cU$ versus U/c. For example, compare the plot at the upper left of Fig. 4 with the corresponding three-dimensional plots. Note, however, that the dimensionless pressure $p/\rho cU$ in Fig. 4 is presented on a linear scale, which differs from the logarithmic scale representation of $p/\rho cU$ in those three-dimensional plots. It is evident by examination of the isometric representations of Fig. 3(b) that three well-defined (major) pressure response peaks can be identified. They all correspond to the first hydrodynamic mode $h1$ and, furthermore, lie along the crests representing the second, third, and fourth acoustic modes, i.e., $a2$, $a3$, and $a4$. These three pressure response peaks are so designated in the upper left plot of Fig. 4. The representations of the plot in the upper left of Fig. 4 are based on curve fits through the data represented in Fig. 3(b). A similar type of representation holds for the remaining five plots given in Fig. 4.

The advantage of this particular type of representation is that it allows a direct comparison of the peak amplitudes of the dimensionless pressure response for increases in cavity length L. It also allows a direct comparison of the values of dimensionless inflow velocity U/c at which each of the peaks occurs. For example, consider the top and middle plots as shown in the left column of Fig. 4, which correspond to two different values of cavity length L. It is evident that the longer cavity length $L = 25.4\,\text{mm}$ allows much larger amplitude peaks, relative to the peak amplitudes at $L = 19.1\,\text{mm}$. In addition, each of the mode combinations at $L = 25.4\,\text{mm}$, i.e., $h1a2$, $h1a3$, and $h1a4$ require a higher value of U/c to generate the peak values. Furthermore, note that at successively larger values of $L = 38.1$, 44.5, 50.8, and 76.2 mm, the peak corresponding to the mode combination of $h1a2$, for example, occurs at successively larger values of U/c. It is interesting to observe, however, that the peak magnitude of this $h1a2$ mode combination does not continue to increase with successively larger values of L and thereby larger values of U/c. Rather, it appears to saturate at about a level of $p/\rho cU = 0.066$ at $L = 25.4\,\text{mm}$ and, after small undulation with increasing L, experiences a substantial drop at $L = 76.2\,\text{mm}$. This abrupt drop at $L = 76.2\,\text{mm}$ occurs in conjunction with the onset of the special mode combination $h1^*a1$, as well as increasingly larger contributions from the second hydrodynamic mode $h2$, principally in the form of $h2a3$ and $h2a4$. Finally, it should be noted that the behavior of the pressure response of mode $h1a2$ described in the foregoing is generally replicated by other mode combinations, such as $h1a1$, $h1a3$, and $h1a4$, especially the increase in value of U/c to excite them at increasing values of streamwise length L of the cavity. At the largest cavity length $L = 76.2\,\text{mm}$, the peaks at $h1a1$, $h1a3$, and $h1a4$ are no longer detectable. Rather, the peak of this threshold mode $h1^*a1$ dominates, along with the peaks at the second hydrodynamic mode, i.e., $h2a1$, $h2a3$, and $h2a4$.

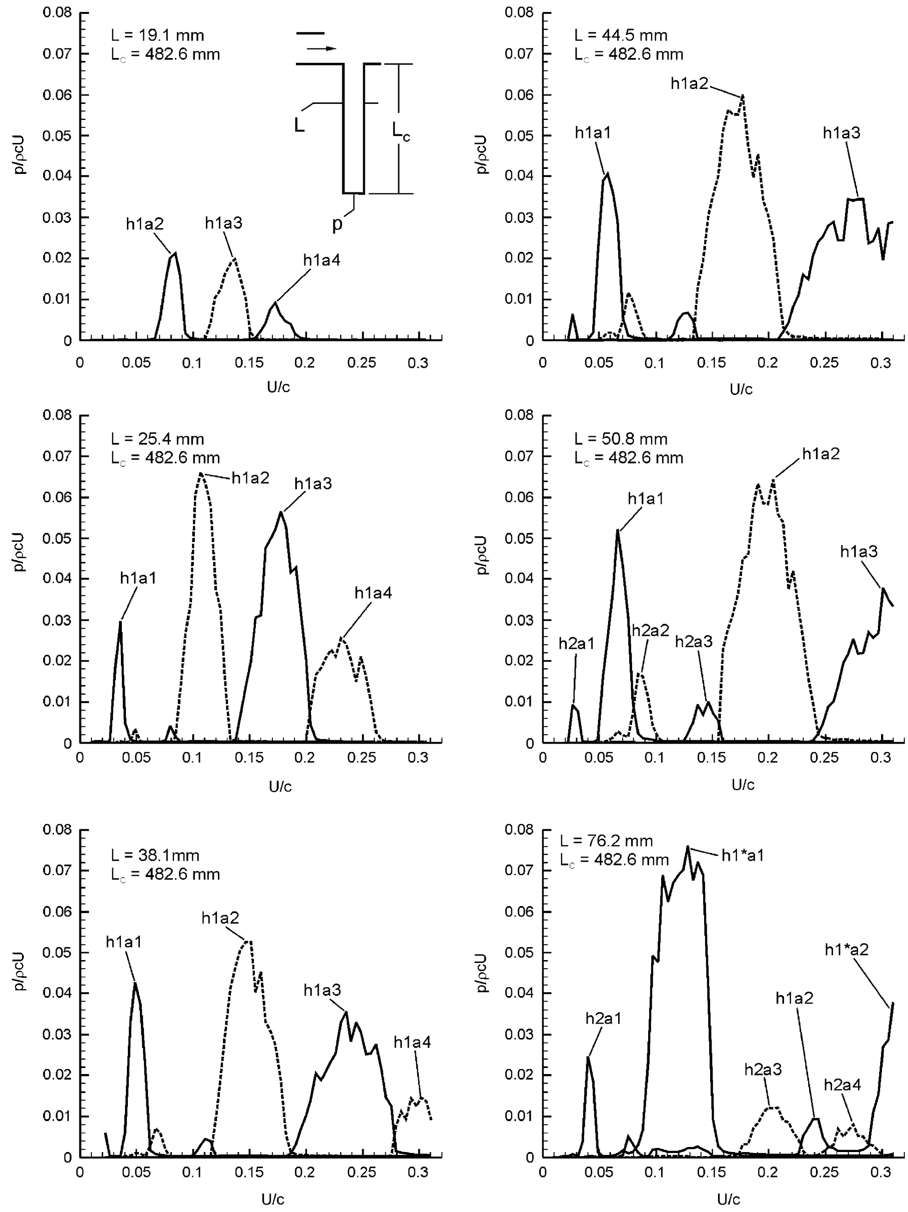

Fig. 4. Variation of dimensionless pressure amplitude $p/\rho cU$ at the end of the deep cavity with dimensionless velocity U/c for the first $h1$ and the second $h2$ hydrodynamic modes and the first through the fourth acoustic modes $a1$, $a2$, $a3$, and $a4$. Each plot corresponds to a different value of streamwise length L of the cavity opening.

Table 1 gives an overview of the parameters corresponding to the peaks of Fig. 4. For each combination of a hydrodynamic mode and an acoustic mode, such as the first hydrodynamic mode (stage) $h1$ and the first acoustic mode $a1$, the following parameters are designated: dimensionless inflow velocity U/c normalized by speed of sound c (Mach number); dimensionless frequency fL/c (Helmholtz number); dimensionless frequency fL/U (Strouhal number); dimensionless frequency $f\theta/U$ based on momentum thickness θ of the inflow; dimensionless pressure amplitude $p/\rho cU$ normalized by inflow velocity U and speed of sound c; dimensionless pressure amplitude normalized by the free stream dynamic head $p/\frac{1}{2}\rho U^2$; and strength of lock-on SoL (definition and detailed discussion are provided in Section 4).

Table 1
Modes and parameters corresponding to the plots of Fig. 4

L (mm)	Mode	U/c	fL/c	fL/U	$f\theta/U$	$p/\rho cU$	$p/\frac{1}{2}\rho U^2$	SoL (dB)
19.1	$h1a2$	0.084	0.029	0.341	0.0105	0.0212	0.503	50.2
	$h1a3$	0.137	0.048	0.348	0.0098	0.0197	0.287	51.1
	$h1a4$	0.173	0.067	0.385	0.0103	0.0092	0.107	47.2
25.4	$h1a1$	0.035	0.013	0.357	0.0098	0.0296	1.670	48.7
	$h1a2$	0.106	0.038	0.358	0.0079	0.0661	1.242	58.3
	$h1a3$	0.177	0.064	0.359	0.0072	0.0564	0.636	57.0
	$h1a4$	0.230	0.088	0.384	0.0073	0.0255	0.221	52.0
50.8	$h1a1$	0.067	0.025	0.372	0.0045	0.0523	1.571	51.6
	$h1a2$	0.204	0.074	0.365	0.0035	0.0644	0.631	50.1
	$h1a3$	0.301	0.123	0.409	0.0037	0.0378	0.251	42.9
	$h2a1$	0.030	0.025	0.925	0.0136	0.0094	0.705	39.1
	$h2a2$	0.084	0.074	0.886	0.0102	0.0168	0.398	45.9
	$h2a3$	0.146	0.125	0.854	0.0089	0.0101	0.138	40.6
76.2	$h1{*}a1$	0.137	0.037	0.271	0.0019	0.0722	1.049	48.9
	$h1a2$	0.244	0.109	0.449	0.0028	0.0094	0.077	29.3
	$h2a1$	0.040	0.037	0.919	0.0083	0.0246	1.233	45.0
	$h2a3$	0.208	0.186	0.892	0.0058	0.0121	0.116	36.5
	$h2a4$	0.275	0.258	0.940	0.0057	0.0080	0.058	33.4

Mode $h1a1$ represents the coincidence of the first hydrodynamic mode (first stage) $h1$ of oscillation of the shear layer and the first acoustic mode $a1$ of the deep cavity. A similar designation holds for other hydrodynamic and acoustic modes. For each of these combinations, dimensionless values of frequency f and amplitude p of each respective spectral peak are tabulated. In addition, values of strength of lock-on SoL are given.

4. Background level of pressure fluctuation and strength of lock-on

In Section 3, emphasis has been on the description of the organized peaks of pressure fluctuations that emerge above the background. These peaks, pronounced or not, are evident in the three-dimensional plots of the respective images of Figs. 3(a)–(e). An issue herein is how to measure the strength of flow tones represented by these peaks. Mendelson (2003) discusses in detail three methods. The first one is to subtract, on a decibel scale, the nonlinear modal response of the resonator to broadband flow noise from the resonant response during occurrence of a flow tone. The second method is to evaluate the quality factor Q of the pressure spectrum. The third is to define the strength in terms of the difference on a decibel scale between the peak of the pressure spectrum and the local broadband level of the spectrum.

Among these three methods, Mendelson (2003) states that the first one is the most tractable, as it is relatively easy to implement. The second method, while a valid measure, involves uncertainties due to finite resolution in the frequency domain; yet, it can be employed as an insightful approximation. Rockwell et al. (2003) address this issue. The third method is difficult to apply, since the local broadband spectral response is largely governed by the location of the transducer.

In the following, efforts are dedicated to application of the first measure, which is designated as strength of lock-on SoL. In addition, a brief comparison between the first and the second measures is made at the end of this section.

4.1. Evaluation of background level

When a resonator is excited only by broadband turbulence, it produces a response amplitude peak in the spectrum whose peak amplitude follows dimensionless velocity U/c raised to a power n. Such broadband flow noise is known to act as a quadrapole (Lauchle, 1992). Experimentally, it has been shown that the power n can be affected by many factors, including the geometric parameters of the resonator and resonant frequencies, as well as the properties of the fluid. In general, with all these conditions fixed, the response in decibels is governed by a linear relation:

$$\text{Response (dB)} = \text{constant} + 20n\,\log(U/c).$$

On a plot of response in decibels versus log of dimensionless velocity, the above would appear as a straight line of slope $20n$. This straight line is referred to as background level, or broadband flow response.

During flow-acoustic coupling, the nonlinear interaction between acoustic and hydrodynamic modes generates a modal response that emerges above the background level. In this case, a linear fit through those data points corresponding to decoupled response can be taken to represent this broadband flow response.

In order to systematically study the behavior of broadband flow response for turbulent shear flow past a deep cavity, plots of peak pressure amplitude p (in decibels) versus inflow velocity U on a logarithmic scale were considered. Each plot of this type corresponds to a selected acoustic mode of a specific deep cavity. All the responses of the deep cavities discussed in Section 3 were evaluated from this perspective. For each cavity configuration, only a limited number of acoustic modes were selected for process, without losing generality.

Fig. 5 shows typical plots. The plots of the left column correspond to selected acoustic modes of cavity having length $L = 25.4\,\text{mm}$ and depth $L_C = 482.6\,\text{mm}$, and the right column to modes of cavity having length $L = 50.8\,\text{mm}$ and depth $L_C = 482.6\,\text{mm}$. In fact, each of these plots is related to a crest of the three-dimensional representation of dimensionless pressure amplitude in Figs. 3(c) and (d), which show dimensionless pressure amplitude on a logarithmic scale as a function of dimensionless frequency and velocity for a designated deep cavity. Each crest occurs for a given resonant acoustic mode along a narrow band of dimensionless frequency; the central value of this band is regarded as the dimensionless frequency of this resonant acoustic mode.

Based on such plots of p (in decibels) versus U/c on logarithmic scale, a linear fit can be made for each plot, using the approach discussed in the foregoing, to indicate the background level represented by each reference line. These fits are represented by the straight lines of Fig. 5. It is evident that, for different acoustic modes of the same cavity, and for different cavities, the background level differs. A general form of the background level is given by

$$p_{BB} = p_{BB0} + 20n\log_{10}(U/c),$$

where p_{BB} denotes the pressure amplitude of the broadband flow response, p_{BB0} is the value of p_{BB} at $U/c = 1$, and $20n$ is the slope of the linear fit, or, specifically, n denotes the exponent to U/c, keeping in mind that $(U/c)^n \propto p_{BB}$.

For all deep cavities and all selected acoustic modes, systematic evaluation of the amplitude p_{BB0} and exponent n was conducted following the approach indicated in Fig. 5. Then, in combination with a curve fitting technique, a series of empirical formulas were developed to predict, both p_{BB0} and n. Further study showed that these two parameters are a function of acoustic mode number n_a, cavity length L, and effective cavity depth L_{eff}. Detailed deduction and formularization are provided by Yang (2005).

4.2. Overview of flow tones based on strength of lock-on

Utilizing the empirical formulas discussed in the foregoing, it is possible to estimate the background level for a specified acoustic mode of a given cavity. The strength of lock-on SoL is defined as follows. It is the difference, on a decibel scale, between the nonlinear modal response of the resonator and the background level (broadband flow response). Values of SoL were determined for all of the cavities discussed in Section 3 and for all of the detectable peaks of each cavity response.

To identify the occurrence of resonant flow tones, two criteria can be employed. The first involves the quality Q factor of the predominant peak in the response spectrum of the pressure fluctuation, as discussed in Section 3; the other is the strength of lock-on SoL criterion, defined in the foregoing. In this part of the investigation, the SoL criterion is employed. In essence, this SoL threshold is established as 40 dB. For purposes of comparison, based on a relatively large set of data acquired herein, SoL = 40 dB generally corresponds to a range of the quality factor of $Q = 250$–500 and to the range of raw pressure amplitude $p = 50$–$200\,\text{Pa}$. Furthermore, it corresponds to the following ranges of dimensionless pressure amplitude response $0.04 \leqslant p/\frac{1}{2}\rho U^2 \leqslant 0.2$ and $0.004 \leqslant p/\rho Uc \leqslant 0.02$.

Upon attainment of the strength of lock-on SoL and establishment of resonance criterion, a three-dimensional bar graph was created on the plane of cavity length L and the ratio of the acoustic mode number n_a to the hydrodynamic mode number n_n, in order to show the flow tone distribution of the entire cavity series, as presented in Fig. 6. The acoustic mode number n_a represents the number of quarter waves along the cavity depth. Referring to Fig. 2(a), for $a1$, $a2$, and $a3$ modes, $n_a = 1$, 3, 5, respectively. In contrast, the hydrodynamic mode number represents the number of large-scale vortices along the cavity mouth, as illustrated in Fig. 2(c), for $h1$ and $h2$ modes, $n_h = 1$ and 2.

In order to easily interpret the bar graph, or cone-like graph representation, given in Fig. 6, it is helpful to clarify the following points:

(i) The bar graph representation is for one series of cavities, and within the series, a given cavity is represented by a shaded strip on the horizontal (bottom) plane.

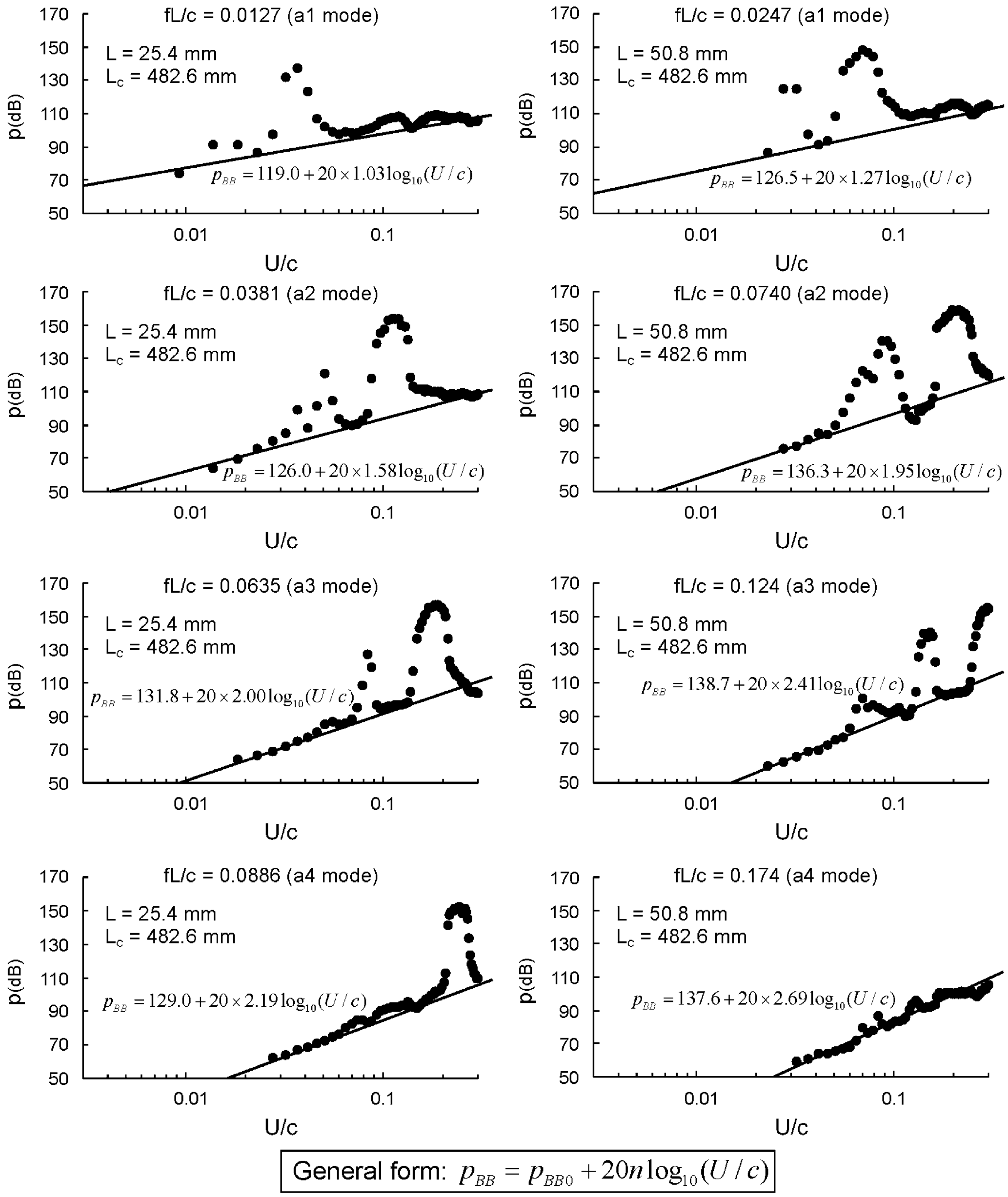

Fig. 5. Variation of pressure amplitude p at the end of the deep cavity as a function of dimensionless velocity U/c relative to a reference line designated as p_{BB}, used for defining the strength of lock-on SoL.

(ii) On a given horizontal shaded strip, each intersection of two solid lines represents the coexistence of the first hydrodynamic mode $h1$ and a given acoustic mode. That is, all peaks related to the $h1$ mode are located at such intersections. Furthermore, these $h1$ modes are further designated by the dark green cone. On the other hand, each intersection of two dashed lines represents the coexistence of the second hydrodynamic mode $h2$ and an acoustic mode, and all peaks related to the $h2$ mode must be located at these intersections. Furthermore, these $h2$ modes are designated by the yellow cone. It should be noted that all possible peaks related to the third and higher hydrodynamic modes are not presented in this bar graph representation, since they were typically of much smaller amplitude.

(iii) Along the right edge of each plot, the ratio of the acoustic mode number to the hydrodynamic mode number is represented by n_a/n_h. These values are given as $n_a/n_h = 1, 3, 5, \ldots$. Keeping in mind that the dark green cone

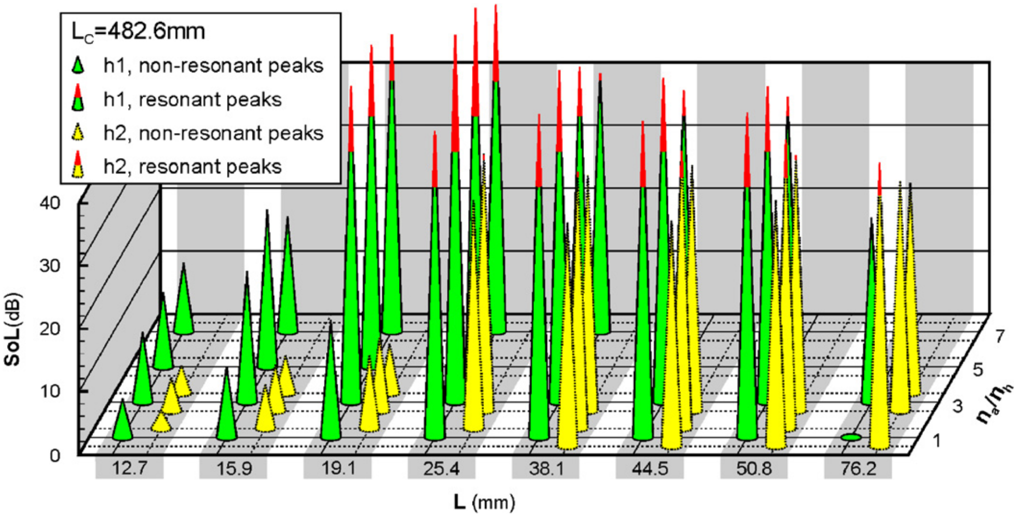

Fig. 6. Representations of strength of lock-on SoL as a function of ratio of acoustic mode number n_a to hydrodynamic mode number n_h and the length L of the cavity opening. Symbols $h1$ and $h2$ correspond to the first and the second hydrodynamic modes (stages), with $n_h = 1$ and 2, respectively. Cavity depth corresponds to $L_C = 482.6$ mm.

corresponds to an $h1$ mode with $n_h = 1$ and the yellow cone corresponds to the $h2$ mode with $n_h = 2$, the acoustic mode number n_a can be evaluated based on the indicated ratio n_a/n_h.

(iv) For a given cavity, i.e., a given strip along the horizontal (bottom) plane, further study shows that the ratio of the acoustic mode number n_a to the hydrodynamic mode number n_h is proportional to the dimensionless inflow velocity U/c. This means that for all of the cones of different colors located on the same shaded strip, the ratio n_a/n_h increases with an increase of U/c. Note, however, that the value of U/c required to excite a mode at a given ratio n_a/n_h is different for each shaded strip on the horizontal (bottom) plane.

(v) Finally, amplitudes that exceed a threshold value of 40 dB are taken to represent a locked-on flow tone, i.e., a resonant peak. Such resonant peaks are presented by green or yellow cones with red tips, whereby the vertical extent of the red region represents the excess of the strength of lock-on SoL relative to the threshold of 40 dB.

As shown in Fig. 6, it is evident that with an increase of the length L of the cavity opening, the strongest attainable strength of lock-on SoL reaches a maximum, then starts to decrease. More specifically, for the peaks related to the first hydrodynamic mode $h1$, there is no locked-on flow tone generated for $L \leqslant 15.9$ mm; for $L \geqslant 19.1$ mm, locked-on flow tones start to occur, and the most pronounced one is observed at $L = 25.4$ mm. In contrast, for those peaks related to the second hydrodynamic mode $h2$, locked-on flow tones first occur at $L = 25.4$ mm and show a peak at $L = 50.8$ mm.

The physics behind the foregoing patterns of peaks for both hydrodynamic modes is as follows. During the interaction, or coupling, of an acoustic mode with a hydrodynamic mode, the fluctuating shear layer needs a sufficient streamwise length to adequately develop. For small values of L, the fluctuation of the shear layer is suppressed, and the response is weak. As L increases, the fluctuation becomes more amplified, yielding larger amplitude response, represented by higher values of SoL. This trend continues until the value of SoL reaches a maximum. The value of L corresponding to this maximum is herein referred to as the optimal length of the cavity opening for generation of flow tones. After that, a further increase of L does not cause a remarkable change of the peak pressure amplitude p, but the intersection of the same acoustic mode with the same hydrodynamic mode will occur at a higher inflow velocity U, which provides a higher background level, and consequently yield a lower value of SoL. Furthermore, for the $h2$ mode, the optimal length L of the cavity opening is twice as large as for the $h1$ mode, since it is expected that two wavelengths of the fluctuating shear layer fit in the streamwise length of the cavity opening for the $h2$ mode instead of one wavelength for the $h1$ mode.

Comparison of the SoL for different hydrodynamic modes shows that, for a given deep cavity, the $h1$ mode is always predominant over other hydrodynamic modes. On each shaded strip, peaks in dark green are generally much higher than peaks in yellow, no matter whether they are resonant or not. Yet, an exception is observed. For the deep cavity of depth $L_C = 482.6$ mm and length $L = 76.2$ mm, an $h1$ mode, $h1a1$, should be preferentially excited, but is missing, as marked by a dark blue ellipse in the bar graph. Although another $h1$ mode $h1a2$ is detected, the value of the SoL is

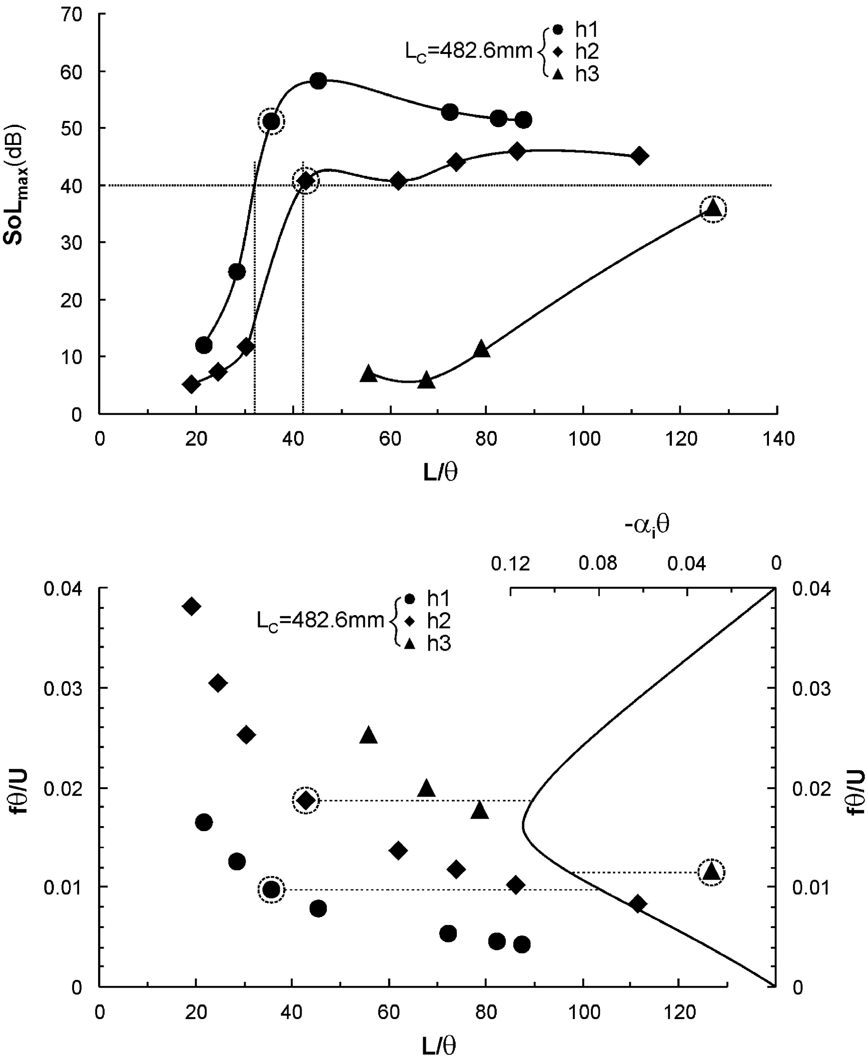

Fig. 7. Variation of strength of lock-on $\mathrm{SoL_{max}}$ at the maximum deviation of pressure amplitude from the reference line as a function of streamwise length L of the cavity opening normalized by the momentum thickness θ of the inflow boundary layer (top plot), and variation of dimensionless frequency $f\theta/U$ as a function of L/θ (bottom plot) in comparison with theoretically determined value of normalized amplification factor $-\alpha_i\theta$ versus $f\theta/U$ [from Michalke (1965)]. The cavity depth is of a fixed value $L_C = 482.6\,\mathrm{mm}$.

much lower than the $h2$ modes. The reason behind this irregular behavior is occurrence of an extension of the $h1$ mode, which has a much lower frequency $h1^*$, as discussed in the foregoing Section 3.

The top plot of Fig. 7 shows the strength of lock-on $\mathrm{SoL_{max}}$, which represents the strongest flow tone for a designated hydrodynamic mode h of a given cavity, as a function of dimensionless streamwise length L/θ of the cavity, in which θ is the momentum thickness of the inflow boundary layer. Three different curves are shown, each for a given hydrodynamic mode $h1$, $h2$, and $h3$. For each view of h, when L/θ becomes sufficiently small, the magnitude of $\mathrm{SoL_{max}}$ becomes very small. For the lowest two hydrodynamic modes, $h1$ and $h2$, rapid increases of $\mathrm{SoL_{max}}$ occur in the range of L/θ from approximately 20 to 45. The values of $\mathrm{SoL_{max}}$ exceed the threshold value of 40 dB in the range of L/θ from 32 to 42, then appear to plateau. In contrast, the corresponding variation for the third hydrodynamic mode $h3$, for which approximately three wavelengths of the instability along the cavity length L occur, shows a much milder variation with L/θ and, furthermore, this mode $h3$ is apparent only at a sufficiently large value of L/θ.

The magnitude of the dominant mode h_1 increases from 11.9 to 40 dB over low values of L/θ. Over this range of L/θ, the corresponding values of quality factor Q, determined from white noise excitation, vary by 3.8% from the nominal value of $Q = 52$. Larger deviations of Q occur at larger L/θ, for which there is onset of nonlinear distortion and saturation of the curve of SoL versus L/θ.

It should be emphasized that the very rapid increase in amplitude, i.e., magnitude of SoL, over a small range of L/θ, as shown in Fig. 7, is very similar to previously documented, purely hydrodynamic oscillations in jet-edge and cavity configurations. For the jet-edge configuration, this phenomenon is depicted in the data of Powell (1961) and Lin and Rockwell (2001). More directly related to the present investigation is the abrupt onset of oscillations in a mixing layer-edge system investigated by Ziada and Rockwell (1982) and the shear-layer along a cavity characterized by Knisely and Rockwell (1982). In both of these systems, the oscillation rises from one-half to its peak value over an incremental length $\Delta L/\theta = 7$ and 8, respectively. For the data Fig. 7, the major share of the increase of SoL occurs within a distance of the order of $\Delta L/\theta = 10$.

Regarding the value of L/θ for the onset of oscillation, represented by the magnitude corresponding to one-half peak magnitude, it is at $L/\theta = 34$ in the investigation of Ziada and Rockwell (1982) and $L/\theta = 57$ in the study of Knisely and Rockwell (1982). In the present investigation, the values of L/θ for onset, using the same criterion, are $L/\theta = 32$ and 42 for the $h1$ and $h2$ modes, respectively.

The lower plot of Fig. 7 shows the corresponding dimensionless frequency $f\theta/U$ as a function of L/θ. These variations are shown for the three hydrodynamic modes $h1$, $h2$, and $h3$. At the right of this plot, the dimensionless amplification factor $-\alpha_i\theta$ versus $f\theta/U$, taken from Michalke (1965), is plotted in such a fashion that one can compare directly with the experimentally observed values of $f\theta/U$, i.e., with the filled circle, diamond and triangular symbols. It is interesting to compare the values of L/θ at which a threshold value of $\mathrm{SoL}_{\max}$ is attained in the top plot of Fig. 7. These values are designated by the dashed circles surrounding the indicated data points, all of which occur in the vicinity of the aforementioned cut-off criterion $\mathrm{SoL}_{\max} \geqslant 40\,\mathrm{dB}$. If these encircled data points are compared with the corresponding encircled points in the bottom plot of $f\theta/U$, it is evident that all three of these dimensionless frequencies fall in a range that corresponds to a relatively large set of values of $-\alpha_i\theta$. If a lower value of cut-off, e.g., $\mathrm{SoL}_{\max}$ is selected, e.g., 20 dB, and one employs interpolation on the curves of Fig. 7, then the intersection of each of the $\mathrm{SoL}_{\max}$ curves with the 20 dB horizontal line yields values of $f\theta/U$ that still occur within a band associated with the most amplified frequencies minus $\alpha_i\theta$. It is useful to keep in mind that, for purely hydrodynamic oscillations of impinging flows, in absence of acoustic effects, it is well known that successive stages, i.e., hydrodynamic modes $h1$, $h2$, and $h3$ are induced by increases of streamwise length L/θ of the cavity opening. At discrete values of L/θ, jumps of the oscillation frequency occur, such that values of $f\theta/U$ remain within the band of sufficiently amplified frequencies according to the plot of Michalke (1965), given in Fig. 7. Bruggeman (1987) demonstrated the relevance of the analysis of Michalke (1965) to these problems to a flow-acoustic-coupled oscillation past a deep cavity, which is part of a pipe system. The principal finding was that when the value of $f\theta/U$ exceeded 0.04, the amplitude of the oscillation was substantially attenuated.

4.3. Comparison of measures of strength of flow tones

For the plots of pressure amplitude p in dB versus dimensionless inflow velocity U/c on a logarithmic scale, as shown in Fig. 5, subtraction of the background level p_{BB} (in dB) from p (in dB) yields another family of plots: strength of lock-on SoL versus dimensionless inflow velocity U/c. Unlike previous descriptions, which focus only on local peaks, the new plots show more details of low-level response, as well as the development of peaks. As an effective measure of the strength of flow tones, a typical representation of variation of SoL as a function of U/c for the first through the fourth acoustic modes $a1$ through $a4$ is provided in Fig. 8, which is related to the deep cavity of length $L = 25.4\,\mathrm{mm}$ and depth $L_C = 482.6\,\mathrm{mm}$. As an alternative measure, the variation of corresponding values of quality factor Q as a function of U/c is also provided in this figure.

Comparison of the profile of SoL with the profile of Q shows that they generally agree well, especially in describing the development of the local peaks. These peaks are marked by the dashed lines on each plot. Each peak represents an intersection between a designated acoustic mode, e.g., $a1$, and the first $h1$ or the second $h2$ hydrodynamic mode. The $h1$ mode peaks occur at relatively high velocities, and the $h2$ mode peaks occur at lower velocities, if they are detectable.

Instead of the foregoing comparison between the two measures, a quantitative comparison can also be made by computing the Q factor in decibels relative to a reference level. Mendelson (2003) suggests that in order to obtain agreement on both measures, it is necessary to choose an appropriate reference for the Q factor. This reference Q factor should be derived from a case without flow-acoustic coupling. However, preliminary experiments, which were conducted by means of white noise excitation and spoiled shear flow past the deep cavity, showed that values of such Q factor varied significantly. Therefore, it is difficult to establish a criterion to choose such a reference level.

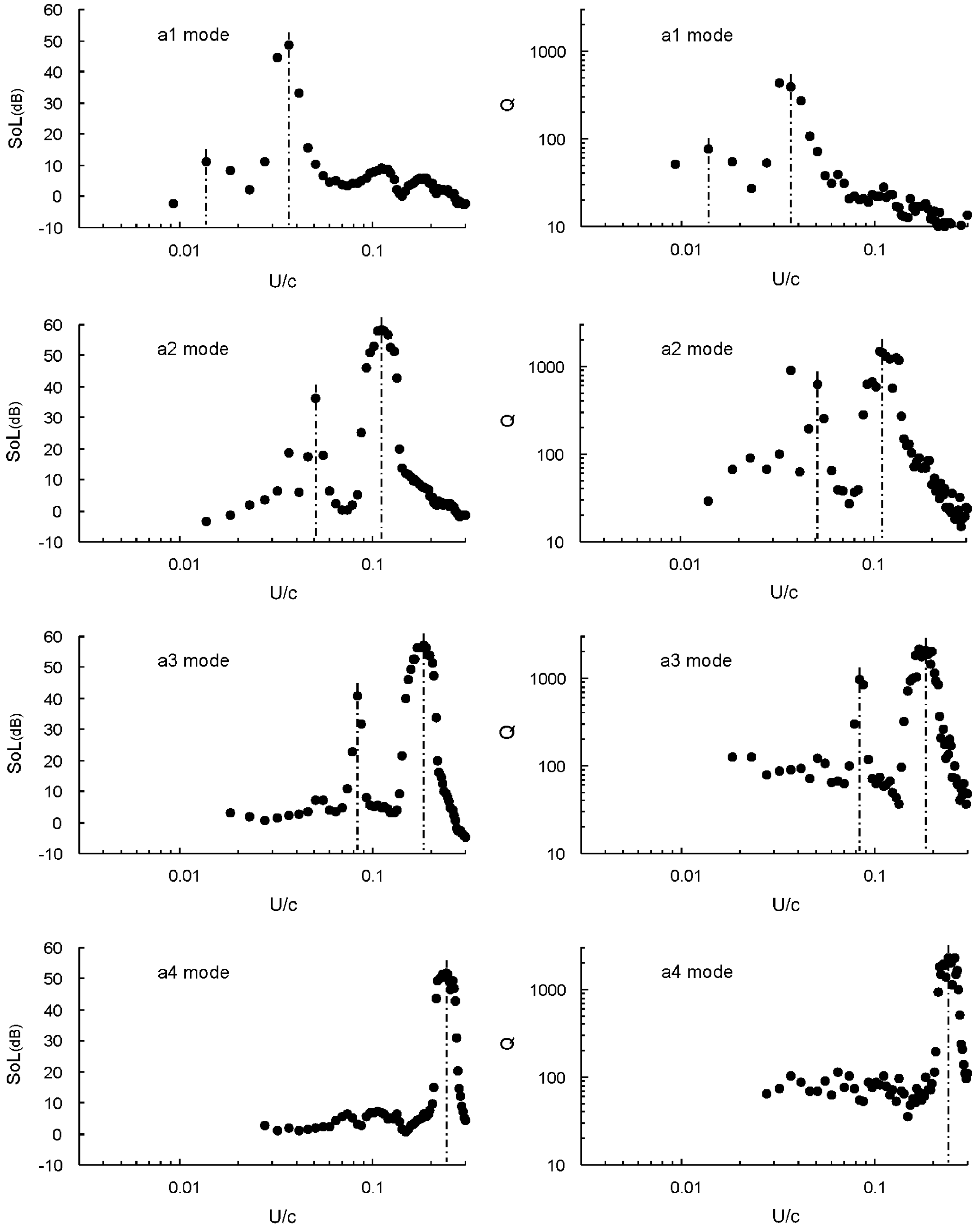

Fig. 8. Strength of lock-on SoL as a function of dimensionless velocity U/c in comparison with corresponding values of quality factor Q as a function of U/c for the first through the seventh acoustic modes $a1$ through $a4$. Streamwise cavity length $L = 25.4\,\text{mm}$, cavity depth $L_C = 482.6\,\text{mm}$.

Taken together, the similar trends of the parameters SoL and Q verifies that both measures are equivalent; the difficulty of evaluating the Q factor in dB relative to a reference level makes the SoL measure a better choice.

As a complement to use of the foregoing criteria of SoL and Q, the occurrence of pronounced higher harmonics at lock-on can be assessed. If one considers the values of U/c at which lock-on occurs in Fig. 8, i.e., values of U/c at which peaks of SoL and Q occur, they correspond to values of U/c at which higher harmonics are prevalent, in the plots of Figs. 3(b)–(e).

5. Conclusions

Tones arising from flow past a deep cavity have been investigated for the case where the cavity functions as an isolated element, i.e., the possibility of coupling with an inflow or outflow duct is precluded. Variations of the streamwise length of the cavity opening, the cavity depth, and the dimensionless inflow velocity provide the potential for coupling between a range of resonant modes of the cavity and hydrodynamic modes of the separated shear layer along the cavity opening.

The principal findings are listed below:

(i) Criteria for onset of a locked-on flow tone have been assessed. They involve the quality factor Q of the spectral peak of the pressure response, and the strength of lock-on SoL, which represents the excess amplitude of the spectral peak with respect to the background noise level. Variations of Q and SoL with dimensionless velocity show remarkably similar forms. Moreover, the dimensionless velocity for occurrence of a flow tone is essentially the same for the Q and SoL criteria.

(ii) Variations of either the dimensionless inflow velocity or the streamwise length of the cavity lead to generation of one of three hydrodynamic modes $h1$, $h2$, and $h3$. Quantitative imaging shows that these modes correspond, respectively, to one, two and three vortical structures along the shear layer, which arise in spite of the fact that the inflow boundary layer is turbulent. In turn, these hydrodynamic modes h can effectively couple with one of four acoustic modes a of the deep cavity.

(iii) Over ranges of streamwise length L of the cavity and dimensionless inflow velocity U/c, coupling of the first hydrodynamic mode $h1$ with one of the possible acoustic modes a nearly always yields the largest amplitude peaks of pressure response, even for relatively long cavity lengths. Moreover, when the streamwise length of the cavity is sufficiently large, an extension $h1^*$ of the first hydrodynamic mode $h1$ occurs. It can lead to large amplitude pressure peaks and a substantially lower dimensionless frequency fL^*/U, presumably due to large amplitude excursions of the separated shear layer into the cavity.

(iv) In contrast, coupling between the third hydrodynamic mode $h3$ and one of the possible acoustic modes a generates peak amplitudes of pressure response that are one to two orders of magnitude smaller than those attainable due to coupling with either the first $h1$ or second $h2$ hydrodynamic mode, over ranges of streamwise length L of the cavity and dimensionless inflow velocity U/c.

(v) Higher harmonics of flow tones are detectable for coupling with both the first and second hydrodynamic modes $h1$ and $h2$. Although these harmonics are sharply defined, the peak amplitude of the first overtone is at least one to two orders of magnitude smaller than the fundamental.

(vi) For sufficiently small streamwise length L of the cavity, below a minimum value designated as $L_{\min}$, normalized by momentum thickness θ, no flow tones are possible. The values lie in the range $32 \leqslant L_{\min}/\theta \leqslant 42$ for the predominant hydrodynamic modes (stages) of the oscillation. These values approximate the minimum values of $L_{\min}/\theta$ for onset of purely hydrodynamic oscillations in impinging mixing layer and cavity flow systems without acoustic effects.

(vii) Onset of the flow tone above a minimum value of $L_{\min}/\theta$ is characterized by a very rapid rise of the pressure amplitude over a relatively small increment of dimensionless streamwise length normalized by inflow momentum thickness θ, i.e., $\Delta L/\theta \cong 10$. A very similar rise of pressure or force magnitude occurs in purely hydrodynamic systems of impinging free shear flows in absence of acoustic effects, over similarly small values of $\Delta L/\theta$.

(viii) The dimensionless frequencies $f\theta/U$, for the data described in (vi) and (vii), lie within the band of highly amplified frequencies according to linear stability theory. Even though the inflow boundary layer is turbulent, the coherent instability emerges above the background level due to acoustic coupling.

(ix) For small values of dimensionless streamwise length L of the cavity, where flow tones are not attainable, mild peaks are nevertheless detectable, allowing definition of dimensionless frequencies f_iL/U consistent with the bands of fL/U at which tones are generated.

Acknowledgments

The authors gratefully acknowledge the advice of Professor Peter Oshkai, presently at the University of Victoria, while holding a post-doctoral position at Lehigh University.

References

Blake, W.K., 1986. Mechanics of Flow-Induced Sound and Vibration, vols. 1 and 2. Academic Press, Inc., New York.

Bruggeman, J.C., 1987. Flow-induced pulsations in pipe systems. Doctoral Dissertation, Technical University of Eindhoven, The Netherlands.

Bruggeman, J.C., Hirschberg, A., van Dongen, M.E.H., Wijnands, A.P.J., Gorter, J., 1989. Flow induced pulsations in gas transport systems: analysis of the influence of closed side branches. ASME Journal of Fluids Engineering 111, 484–491.

Bruggeman, J.C., Hirschberg, A., van Dongen, M.E.H., Wijnands, A.P.J., Gorter, J., 1991. Self-sustained aero-acoustic pulsations in gas transport systems: experimental study of the influence of closed side branches. Journal of Sound and Vibration 150, 371–393.

Cremer, L., Ising, H., 1967. Die selbsterregten schwingungen von orgelpfeifen. Acustica 19, 143–153.

Cumpsty, N.S., Whitehead, D.S., 1971. The excitation of acoustic resonances by vortex shedding. Journal of Sound and Vibration 18 (3), 353–369.

Davies, P.O.A.L., 1981. Flow–acoustic coupling in ducts. Journal of Sound and Vibration 77 (2), 191–209.

Davies, P.O.A.L., 1996a. Piston engine intake and exhaust system design. Journal of Sound and Vibration 190, 677–712.

Davies, P.O.A.L., 1996b. Aeroacoustics and time varying systems. Journal of Sound and Vibration 190, 345–362.

DeMetz, F.C., Farabee, T.M., 1977. Laminar and turbulent shear flow-induced resonances. AIAA Paper 77-1293.

Dequand, S., Luo, X., Willems, J., Hirschberg, A., 2003a. Helmholtz-like resonator self-sustained oscillations. Part 1: acoustical measurements and analytical models. AIAA Journal 41 (3), 408–415.

Dequand, S., Hulshoff, S., Van Kuijk, H., Willems, J., Hirschberg, A., 2003b. Helmholtz-like resonator self-sustained oscillations. Part 2: detailed flow measurements and numerical simulations. AIAA Journal 41 (3), 416–423.

Dequand, S., Hulshoff, S.J., Hirschberg, A., 2003c. Self-sustained oscillations in a closed side branch system. Journal of Sound and Vibration 265 (2), 359–386.

Elder, S.A., 1978. Self-excited depth-mode resonance for a wall-mounted cavity in turbulent flow. Journal of Acoustical Society of America 64, 877–890.

Flatau, A., Van Moorham, W.K., 1990. Prediction of vortex shedding responses in segmented solid rocket motors. AIAA Paper 90-2073.

Fletcher, N.H., 1974. Nonlinear interactions in organ flue pipes. Journal of the Acoustical Society of America 56 (2), 645–652.

Fletcher, N.H., 1976. Sound production by organ flue pipes. Journal of the Acoustical Society of America 60 (4), 926–936.

Fletcher, N.H., 1979. Air flow and sound generation in musical wind instruments. Annual Review of Fluid Mechanics 11, 123–146.

Geveci, M., Oshkai, P., Rockwell, D., Lin, J.-C., Pollack, M., 2003. Imaging of the self-excited oscillation of flow past a cavity during generation of a flow tone. Journal of Fluids and Structures 18 (6), 665–694.

Ho, C.M., Huerre, P., 1984. Perturbed free shear layers. Annual Review of Fluid Mechanics 16, 365–424.

Hofmans, G.C.J., 1998. Vortex sound in confined flows. Doctoral Dissertation, Technical University of Eindhoven, The Netherlands.

Hourigan, K., Welsh, M.C., Thompson, M.C., Stokes, A.N., 1990. Aerodynamic sources of acoustic resonance in a duct with baffles. Journal of Fluids and Structures 4, 345–370.

Howe, M.S., 1975. Contributions to the theory of aerodynamic sound, with application to excess jet noise and theory of the flute. Journal of Fluid Mechanics 71, 625–673.

Howe, M.S., 1980. The dissipation of sound at an edge. Journal of Sound and Vibration 70, 407–411.

Howe, M.S., 1983. The attenuation of sound in a randomly lined duct. Journal of Sound and Vibration 87 (1), 83–103.

Ingard, U., Singhal, V.K., 1976. Flow excitation and coupling of acoustic modes of a side-branch cavity in a duct. Journal of the Acoustical Society of America 60, 1213–1215.

Jungowski, W.M., Botros, K.K., Studzinski, W., 1989. Cylindrical side-branch as tone generator. Journal of Sound and Vibration 131, 265–285.

Knisely, C., Rockwell, D., 1982. Self-sustained low-frequency components in an impinging shear layer. Journal of Fluid Mechanics 116, 157–186.

Kriesels, P.C., Peters, M.C.A.M., Hirschberg, A., Wijnands, A.P.J., Iafrati, A., Riccaradi, G., Piva, R., Bruggeman, J.C., 1995. High amplitude vortex-induced pulsations in a gas transport system. Journal of Sound and Vibration 184, 343–368.

Lambert, R.F., 1953. A study of the factors influencing the damping of an acoustical cavity resonator. Journal of the Acoustical Society of America 25, 1068–1083.

Lauchle, G.C., 1992. Modern Methods in Analytic Acoustics: Lecture Notes. Springer, Berlin.

Lin, J.-C., Rockwell, D., 2001. Oscillations of a turbulent jet incident upon an edge. Journal of Fluids and Structures 15 (6), 791–829.

Mallick, S., Shock, R., Yakhot, V., 2003. Numerical simulation of the excitation of a Helmholtz resonator by a grazing flow. Journal of the Acoustical Society of America 14 (4), 1833–1840.

Mendelson, R.S., 2003. Methods of measuring lock-in strength and their application to the case of flow over a cavity locking into a single side branch. AIAA Paper 2003-3106.

Michalke, A., 1965. On spatially growing disturbances in an inviscid shear layer. Journal of Fluid Mechanics 23, 521–544.

Nelson, P.A., Halliwell, N.A., Doak, P.E., 1981. Fluid dynamics of a flow excited resonance. Part I: experiment. Journal of Sound and Vibration 78, 15–38.

Nelson, P.A., Halliwell, N., Doak, P.E., 1983. Fluid dynamics of a flow excited resonance. Part II: flow acoustic interaction. Journal of Sound and Vibration 91, 375–402.

Oshkai, P., Geveci, M., Rockwell, D., Pollack, M., 2004. imaging of acoustically coupled oscillations due to flow past a shallow cavity: effect of cavity length scale. Journal of Fluids and Structures 20 (2), 277–308.

Parker, R., 1966. Resonance effects in wake shedding from parallel plates: some experimental observations. Journal of Sound and Vibration 4, 62–72.

Pfizenmaier, E., 1973. On the instability of a sound influenced free jet. E.S.R.O. Technical Transactions no. 122 (Translation of DFVLR Berlin Report DLR-FB 73-69).

Powell, A., 1961. On the edgetone. Journal of the Acoustical Society of America 33, 395–409.

Radavich, P.M., Selamet, A., Novak, J.M., 2001. A computational approach for flow-acoustic coupling in closed side branches. Journal of the Acoustical Society of America 109, 1343–1353.

Ricot, D., Maillard, V., Bailly, C., 2002. Numerical simulation of unsteady cavity flow using lattice Boltzman method. In: Eighth AIAA/CEAS Aeroacoustics Conference and Exhibit, AIAA, Breckenridge, CO, USA, 17–19 June, pp. 2002–2532.

Rockwell, D., 1983. Oscillations of impinging shear layers. Invited Lecture, 20th Aerospace Sciences Meeting of AIAA, January 1981, Orlando, FL, AIAA Paper 81-0047 (also see AIAA Journal 21, 645–664).

Rockwell, D., 1998. Vortex-body interactions. Annual Review of Fluid Mechanics 30, 199–229.

Rockwell, D., Karadogan, H., 1982. Oscillations of an impinging turbulent jet: coherence characterization via conditional sampling. Journal of Sound and Vibration 83 (1), 111–124.

Rockwell, D., Karadogan, H., 1983. Toward attenuation of self-sustained oscillations of a turbulent jet through a cavity. ASME Journal of Fluids Engineering 105 (3), 335–340.

Rockwell, D., Naudascher, E., 1978. Review—self-sustaining oscillations of flow past cavities. ASME Journal of Fluids Engineering 100, 152–165.

Rockwell, D., Naudascher, E., 1979. Self-sustained oscillations of impinging free-shear layers. Annual Review of Fluid Mechanics 11, 67–94.

Rockwell, D., Schachenmann, A., 1982a. Self-generation of organized waves in an impinging turbulent jet at low Mach number. Journal of Fluid Mechanics 117, 425–441.

Rockwell, D., Schachenmann, A., 1982b. The organized shear layer due to oscillations of a turbulent jet through an axisymmetric cavity. Journal of Sound and Vibration 85, 371–382.

Rockwell, D., Lin, J.-C., Oshkai, P., Reiss, M., Pollack, M., 2003. Shallow cavity flow tone experiments: onset of locked-on states. Journal of Fluids and Structures 17, 381–414.

Schachenmann, A., Rockwell, D., 1980. A quasi-standing-wave phenomenon due to oscillating internal flow. ASME Journal of Fluids Engineering 102, 70–77.

Stoneman, S.A.T., Hourigan, K., Stokes, A.N., Welsh, M.E., 1988. Resonant sound caused by flow past two plates in tandem in a duct. Journal of Fluid Mechanics 192, 455–484.

Takeda, K., Shieh, C.M., 2004. Cavity tones by computational aeroacoustics. International Journal of Computational Fluid Dynamics 18 (6), 439–454.

Weaver, D.S., Ziada, S., Au-Yang, M.K., Chen, S.S., Païdoussis, M.P., Pettigrew, M.J., 2000. Flow-induced vibrations in power and process plant components—progress and prospects. ASME Journal of Pressure Vessel Technology 122, 339–348.

Yang, Y., 2005. Generation of tones due to grazing shear flow past a deep cavity. Doctoral Dissertation, Lehigh University.

Ziada, S., Bühlmann, E.T., 1992. Self-excited resonances of two-side-branches in close proximity. Journal of Fluids and Structures 6, 583–601.

Ziada, S., Rockwell, D., 1982. Oscillations of an unstable mixing layer impinging upon a wedge. Journal of Fluid Mechanics 124, 307–334.